applied sciences

MDPI

Article

Fast and Simultaneous Estimation of Thermophysical and Geometric Parameters for Thermal Barrier Coating Systems in High-Temperature Environments via a PCA-Optimized ANN-PSO-Based Accelerated Inverse Model

Yang Liu [1,*], Qi Lang [1], Didier Saury [2] and Denis Lemonnier [2]

[1] Sino-European Institute of Aviation Engineering, Civil Aviation University of China, Tianjin 300300, China; langqi_email@163.com
[2] Institut Pprime, UPR CNRS 3346, CNRS, ISAE-ENSMA, Universite de Poitiers, Futuroscope, 86961 Chasseneuil CEDEX, France; didier.saury@ensma.fr (D.S.); denis.lemonnier@ensma.fr (D.L.)
* Correspondence: yang_liu@cauc.edu.cn

Abstract

In this article, an inverse mathematical model was developed to achieve fast and simultaneous estimation of thermophysical and geometric parameters for thermal barrier coating (TBC) systems in high-temperature environments with measurement errors. First, considering the convective and radiative heat transfer between the TBC system and the external environment, a one-dimensional unsteady conduction–radiation coupled heat transfer model was originally developed in high-temperature environments. Subsequently, this forward model was solved using the finite volume method (FVM), and the grid independence as well as the accuracy were validated. Thereafter, an accelerated inverse model, which adopts a principal component analysis (PCA)-optimized artificial neural network (ANN) to fit and substitute the forward model and employs the particle swarm optimization (PSO) algorithm for estimation, was developed based on the inverse method. Finally, under three different noise conditions, two situations were used to perform simultaneous estimation studies: a two-parameter case (top coat thermal conductivity and thermally grown oxide (TGO) layer thickness) and a three-parameter case (adding the thickness of an additional existing debonding defect layer). The results show that the PCA-optimized ANN-PSO-based accelerated inverse model is approximately 111–130 times faster than the traditional PSO-based inverse model, and the maximum relative errors of the arithmetic means of 20 estimations for two-parameter and three-parameter situations under three noise cases are on the order of 2.4% to 4.3%. Overall, the proposed accelerated inverse model achieves a favorable balance between speed and accuracy in multi-type parameter simultaneous estimation for TBC systems at high temperature, providing a methodological basis for addressing parameter estimation in more complex situations in future research.

Keywords: thermal barrier coating system; multi-type parameters; fast simultaneous estimation; artificial neural networks; principal component analysis; inverse method

Check for updates

Academic Editor: Francesco Zirilli

Received: 27 May 2026
Revised: 2 July 2026
Accepted: 10 July 2026
Published: 14 July 2026

Copyright: © 2026 by the authors. Licensee MDPI, Basel, Switzerland. This article is an open access article distributed under the terms and conditions of the Creative Commons Attribution (CC BY) license.

1. Introduction

Elevating the turbine inlet temperature is a core pathway for augmenting the thrust-to-weight ratio and fuel efficiency of aeronautical propulsion systems, with thermal protection technologies for hot-section components serving as essential means. Thermal

protection technologies can be classified into active and passive categories, where passive thermal protection technology typically achieves thermal insulation via thermal barrier coating (TBC). The prevailing TBC material, yttria-stabilized zirconia ceramic, exhibits a coupled conduction–radiation heat transfer mechanism and is characterized as a typical semi-transparent material. For the TBC system studied, it typically consists of the TBC (sometimes also referred to as the top coat), the bond coat and the substrate. In the high-temperature environment during service, oxygen species permeate the top coat and react with metallic constituents in the bond coat, leading to the formation of the thermally grown oxide (TGO) at the interface. Progressive thickening of the TGO layer to an order of magnitude of 10 μm [1] will probably trigger sequential successive interfacial debonding defects and ultimately results in coating delamination failure. Given that the evolution of the TGO and the interfacial debonding defect are one of the dominant factors leading to TBC systems failure, and the thermal conductivity of the semi-transparent ceramic top coat is a key parameter influencing their evolution, it is essential to conduct fast and simultaneous estimation of the thermal conductivity of the top coat, and the thickness of the interfacial debonding defect layer and the TGO layer. This estimation aims to quantify the thermal insulation performance of TBC systems and capture characteristic information of TGO and debonding defects in their early growth stages, serving as a prerequisite to enable timely warning and precise intervention in TBC systems maintenance. It also constitutes a critical foundation to ensure the efficient and safe operation of aero-engines.

The estimation of the thickness of the debonding defect layer and that of the TGO layer usually relies on non-destructive testing (NDT) techniques, which mainly include acoustic emission technology [2], ultrasonic testing technology [3], eddy current method [4], terahertz time-domain spectroscopy [5,6] and active infrared thermography [7,8]. Such inspections are typically carried out under non-operating conditions, and it is challenging to achieve fast and simultaneous estimation of thermophysical and geometric parameters in TBC systems during service when relying solely on a single technique. Unlike the NDT techniques, the inverse method takes measurement data (such as temperature) under operating conditions as known inputs. Through constructing a forward model that describes system behavior and leveraging mathematical tools like optimization algorithms, it enables the simultaneous estimation of multi-parameters of systems under in-service conditions, ultimately achieving precise description and analysis of complex systems. However, it also places higher demands on the accuracy and solution speed of the forward model.

For the problem studied, the forward model within the inverse method framework is a multi-layer coupled heat transfer model containing the TGO and the debonding defect in high-temperature environments. For the local heat transfer simulation of this model, specifically the radiative heat transfer in the top coat, the primary simulation methods include semi-analytical approaches based on time-domain/frequency-domain Laplace transforms [9,10], photon trajectory-tracking methods (e.g., ray tracing method [11], zonal method, Monte Carlo method [12,13], discrete transfer method [14]), and discretization-based methods (e.g., finite volume method (FVM) [15], finite element method (FEM) [16], discrete ordinate method (DOM) [17], spherical harmonic method [18,19]). These methods exhibit distinct advantages and limitations: semi-analytical methods offer fast computational speed but require mathematical approximations to derive solutions as problem complexity increases; photon trajectory-tracking methods are suitable for radiative calculations involving non-uniform media, anisotropic scattering, complex geometries and variable refractive indices but incur high computational costs when coupled with conduction/convection. In contrast, discretization-based methods have relatively short computation time and are suitable for coupled calculations.

As for the global heat transfer simulation of the forward model, Sun et al. [20] analyzed the temperature response of the coating surface under flashlamp irradiation using a one-dimensional multi-layer heat conduction model. Based on this analysis, they proposed a pulsed thermography analysis method to measure the thermal conductivity and heat capacity distribution of the TBC. Zhu et al. [21] developed a 3D thermo-mechanical coupled model for TBC systems using finite element software. They employed a heat conduction model to study the heat transfer within the TBC systems and predicted coating failure by the stress distribution analysis. Tang et al. [22] developed a 3D heat conduction model for TBC systems and realized non-uniform thickness detection using pulsed thermography technology. Adamczyk et al. [23] developed a 3D heat conduction model for TBC systems and conducted numerical simulations using ANSYS thermal finite element software, ultimately identifying the equivalent thermal conductivity of the TBC via the Levenberg–Marquardt algorithm. Gao et al. [24] proposed a simplified one-dimensional heat conduction model for TBC systems with film cooling and solved it using ANSYS finite element software. Yang et al. [25] developed a simplified heat conduction model for TBC systems with thin semi-transparent ceramic layers (40–120 μm) and then, under short laser pulses, identified the thermal relaxation time of coating using infrared thermography technology to obtain the coating thickness.

Overall, extensive research has been conducted on global heat transfer issues of TBC systems. However, these studies commonly adopt simplified multi-layer heat conduction models and ignore thermal radiation effects within the semi-transparent top coat. Considering that the radiative heat flux in the top coat increases exponentially with high ambient temperature during service, disregarding thermal radiation effects in such scenarios will reduce the accuracy of both local and global heat transfer simulations. Furthermore, the research by Vavilov et al. [26] indicates that in active thermal testing using optical heating, neglecting the translucency of materials will seriously affect the measurement of internal defects in composites.

With the rapid development of artificial neural networks (ANNs), its outstanding analytical and predictive capabilities have gradually made it a critical technical means in the field of NDT of TBC systems. For the high noise and blurred edges problem in pulsed infrared thermography images, Tang et al. [27] proposed a novel edge detection method combining fuzzy C-means clustering and Canny operator, enabling clear and accurate defect edge recognition with high positioning accuracy and robust noise resistance. Tang et al. [28] also developed a quantitative detection method for the diameter and depth of circular flat-bottom debonding defects in TBC systems using pulsed infrared thermography, principal component analysis and BP neural networks. For defects with depths of 1–2.5 mm and diameter-to-depth ratios of 1.2–4.0, the measurement errors for depth and diameter were within 4–10%. Yousefi et al. [29] proposed an eigen-decomposition technique integrating covariance matrix estimation with singular value decomposition to generate principal component thermography results, and improved defect detection efficiency through K-medoids clustering-based segmentation. Luo et al. [30] designed a deep learning network architecture incorporating temporal and spatial information for automated defect segmentation in composites using photoacoustic infrared thermography, which enhanced the contrast between defective areas and normal areas. Luo et al. [31] combined stationary wavelet transform and BP neural networks with terahertz time-domain spectroscopy to effectively predict TGO thickness (1–29 μm) in TBC systems. Ye et al. [32] proposed a novel interface delamination evaluation method integrating terahertz time-domain spectroscopy, BP neural networks and support vector machines, enabling prediction of early-stage interface delamination thickness in TBC systems. Shi et al. [33] developed an algorithm integrating gray-gradient spatial histogram-entropy, multi-threshold

segmentation and stacked restricted Boltzmann machines. The algorithm firstly extracted color/spatial features via histogram-entropy analysis, subsequently performed preliminary crack segmentation using multi-thresholding and finally characterized the length, location and quantity of cracks using the stacked restricted Boltzmann machines. Shi et al. [34] also proposed an NDT technique based on an enhanced multi-scale faster region-based convolutional neural network to detect internal cracks in the TBC and predict remaining coating lifespan. Jaeger et al. [35] utilized deep convolutional neural networks to develop an automated infrared thermography classification program for engine turbine blade defects, improving both classification speed and accuracy.

Overall, for the estimation of the interfacial defect and the TGO using deep learning, current research mainly focuses on two aspects: enhancing the interpretability of experimental data by leveraging the robust analytical capabilities of deep learning networks; and making up for limitations in traditional NDT techniques using the predictive capacities of deep learning. However, research on combining deep learning with inverse methods to estimate the thermophysical properties and geometric parameters of TBC systems still has certain gaps.

In summary, by accounting for thermal radiation in semi-transparent coatings under high-temperature conditions, this article develops a one-dimensional transient multi-layer coupled heat transfer model for TBC systems, thereby theoretically addressing this research gap. Based on this forward model, an accelerated inverse model is presented for fast and simultaneous estimation of the thermal conductivity of the top coat, the thickness of the interfacial debonding defect layer and that of the TGO layer for TBC systems in high-temperature environments. To this end, principal component analysis (PCA) is firstly applied to temperature observations to effectively reduce the output dimension of the neural network and further simplify its structure complexity. Then, by leveraging the instantaneous fitting characteristics of deep learning, the forward simulation process in the inverse model is accelerated, thereby mitigating the limitations of traditional inverse methods in terms of estimation speed. Next, more details will be presented on the development and validation of the forward model, the parameter sensitivity study, the establishment of a PCA-optimized ANN-particle swarm optimization (PSO)-based accelerated inverse model and the results analysis.

2. Forward Model

2.1. Case Study and Associated Forward Model

Figure 1 shows an unsteady heat transfer model of the TBC system studied, which is assumed to consist of a top coat, a debonding defect layer, a TGO layer, a bond coat and a substrate. Both left and right boundaries of the system exhibit convective and radiative heat transfer with the environment. Given that the thickness of each layer is much smaller than its in-plane dimensions, the internal heat transfer within the system is simplified as a one-dimensional process. In addition, the debonding defect layer is modeled as a dry air-filled region which is transparent for thermal radiation.

It is assumed that the homogeneous, emissive, absorptive, isotropic scattering top coat has a thickness of L_1, thermal conductivity λ_1, density ρ_1, specific heat capacity c_1, refractive index n_1, absorption coefficient κ_a and scattering coefficient κ_d, with both its boundary surfaces being diffuse and gray. The temperature of the high-temperature gas on the left side of the top coat is T_{g1} and the convective heat transfer coefficient is h_{g1}. The homogeneous and isotropic debonding defect layer has a thickness of L_2. The heat transfer within it consists of thermal conduction in the air and radiative heat transfer between the right boundary of the top coat and the left boundary of the TGO layer. The subsequent layers (the TGO layer, bond coat and substrate) are all considered as opaque, homogeneous

and isotropic. The temperature of the low-temperature gas on the right side of the substrate is T_{g5} and the convective heat transfer coefficient is h_{g5}. The total thickness of the TBC system is L.

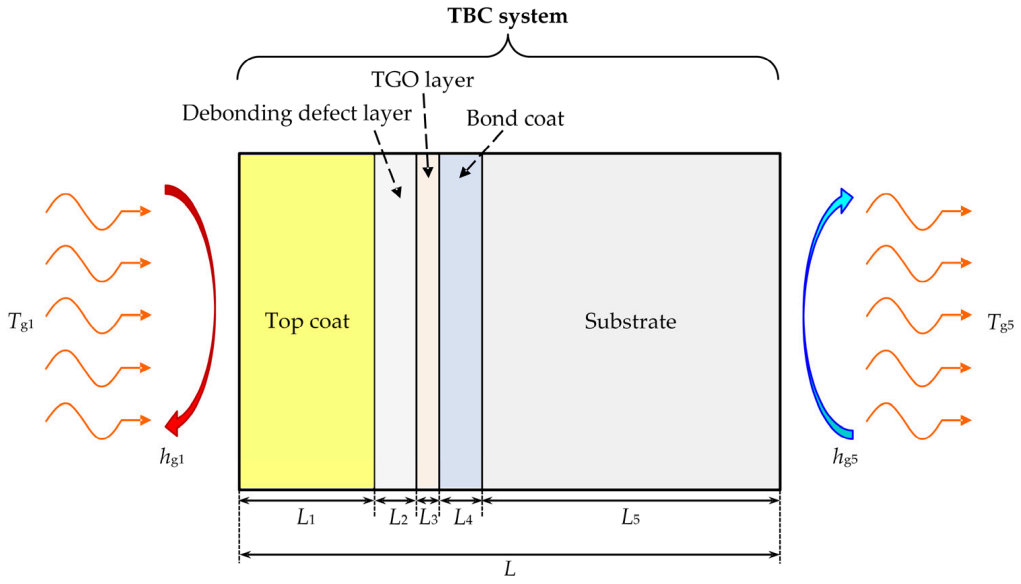


Figure 1. One-dimensional unsteady heat transfer model of the TBC system with a debonding defect layer and a TGO layer.

Based on the P1 approximation [36], the coupled conduction–radiation heat transfer equation describing the heat transfer within the top coat can be written as follows:

$$div\left(\overrightarrow{grad}G\right) = (1 - \omega)3\kappa^2\left(G - 4n_1^2\sigma T_1^4\right) \tag{1}$$

$$\rho_1 c_1 \frac{\partial T_1}{\partial t} = div\left(\lambda_1 \overrightarrow{grad}T_1\right) + div\left(\frac{1}{3\kappa}\overrightarrow{grad}G\right) \tag{2}$$

where $\kappa = \kappa_a + \kappa_d$ is the extinction coefficient, $\omega = \kappa_d/\kappa$ is the albedo, σ is the Stefan–Boltzmann constant, and T_1 and G are respectively the temperature and incident radiation within the top coat.

The air conduction within the debonding defect layer and the solid heat conduction within the TGO layer, the bond coat and the substrate can be described by the heat conduction equation without internal heat sources:

$$\rho_i c_i \frac{\partial T_i}{\partial t} = div\left(\lambda_i \overrightarrow{grad}T_i\right) \qquad i = 2, 3, 4, 5 \tag{3}$$

where ρ_i, c_i, λ_i and T_i respectively represent the density, the specific heat capacity, the thermal conductivity and the temperature of the debonding defect layer ($i = 2$), the TGO layer ($i = 3$), the bond coat ($i = 4$) and the substrate ($i = 5$). The boundary conditions corresponding to Equations (1) and (3) can be derived based on the conservation of heat flux and the continuity of temperature at each boundary:

$$-\lambda_1 \frac{\partial T_1}{\partial x}\bigg|_{x=0} - \frac{1}{3\kappa}\frac{\partial G}{\partial x}\bigg|_{x=0} = h_{g1}\left(T_{g1} - T_1(x = 0)\right) + \varepsilon_{1\text{-}1}\sigma\left(T_{g1}^4 - T_1^4(x = 0)\right) \tag{4}$$

$$\begin{cases} -\lambda_1 \frac{\partial T_1}{\partial x}\Big|_{x=L_1} - \frac{1}{3\kappa}\frac{\partial G}{\partial x}\Big|_{x=L_1} = -\lambda_2 \frac{\partial T_2}{\partial x}\Big|_{x=L_1} + q_r \\ T_1|_{x=L_1} = T_2|_{x=L_1} \end{cases} \tag{5}$$

$$\begin{cases} -\lambda_2 \frac{\partial T_2}{\partial x}\Big|_{x=L_1+L_2} + q_r = -\lambda_3 \frac{\partial T_3}{\partial x}\Big|_{x=L_1+L_2} \\ T_2|_{x=L_1+L_2} = T_3|_{x=L_1+L_2} \end{cases} \tag{6}$$

$$\begin{cases} -\lambda_3 \frac{\partial T_3}{\partial x}\Big|_{x=L_1+L_2+L_3} = -\lambda_4 \frac{\partial T_4}{\partial x}\Big|_{x=L_1+L_2+L_3} \\ T_3|_{x=L_1+L_2+L_3} = T_4|_{x=L_1+L_2+L_3} \end{cases} \tag{7}$$

$$\begin{cases} -\lambda_4 \frac{\partial T_4}{\partial x}\Big|_{x=L_1+L_2+L_3+L_4} = -\lambda_5 \frac{\partial T_5}{\partial x}\Big|_{x=L_1+L_2+L_3+L_4} \\ T_4|_{x=L_1+L_2+L_3+L_4} = T_5|_{x=L_1+L_2+L_3+L_4} \end{cases} \tag{8}$$

$$-\lambda_5 \frac{\partial T_5}{\partial x}\Big|_{x=L} = h_{g5}\left(T_5(x=L) - T_{g5}\right) + \varepsilon_{5\text{-}2}\sigma\left(T_5^4(x=L) - T_{g5}^4\right) \tag{9}$$

where $\varepsilon_{1\text{-}1}$ is the emissivity of the boundary of the top coat exposed to the high-temperature gas ($x = 0$) and $\varepsilon_{5\text{-}2}$ is the emissivity of the boundary of the substrate exposed to the low-temperature gas ($x = L$). Under one-dimensional assumption, the radiative heat flux q_r between the boundary of the top coat at $x = L_1$ and the boundary of the TGO layer at $x = L_1 + L_2$, is modeled as that between two parallel infinite planes and given by:

$$q_r = \frac{\sigma\left[T_1^4(L_1) - T_2^4(L_1 + L_2)\right]}{\frac{1}{\varepsilon_{1\text{-}2}} + \frac{1}{\varepsilon_{3\text{-}1}} - 1} \tag{10}$$

where $\varepsilon_{1\text{-}2}$ is the emissivity of the right boundary of the top coat ($x = L_1$) and $\varepsilon_{3\text{-}1}$ is the emissivity of the left boundary of the TGO layer ($x = L_1 + L_2$).

The boundary conditions for Equation (2) can be described using Marshak boundary conditions:

$$x = 0: -\frac{2}{3\kappa}\frac{2 - \varepsilon_{1\text{-}1}}{\varepsilon_{1\text{-}1}}\frac{\partial G}{\partial x} + G = 4n_1^2\sigma T_1^4 \tag{11}$$

$$x = L_1: \frac{2}{3\kappa}\frac{2 - \varepsilon_{1\text{-}2}}{\varepsilon_{1\text{-}2}}\frac{\partial G}{\partial x} + G = 4n_1^2\sigma T_1^4 \tag{12}$$

The initial conditions for the forward model are:

$$\forall x: T(x, t = 0) = T_{ini} \tag{13}$$

$$\forall x: G(x, t = 0) = 4n_1^2\sigma T_{ini}^4 \tag{14}$$

2.2. Resolution of the Forward Model

The one-dimensional unsteady forward heat transfer model for the TBC system containing a debonding defect layer and a TGO layer can be solved using the FVM. As shown in Figure 2, to ensure the calculation accuracy at the boundaries, the length of the control volumes at the boundaries of each layer is set to half of that of the internal control volumes in the same layer. In the figure, the dashed lines represent the boundaries of the control volumes, and the ellipsis indicates the omitted control volumes. The number of spatial nodes for the top coat, the debonding defect layer, the TGO layer, the bond coat and the substrate are respectively denoted as N_{x_1}, N_{x_2}, N_{x_3}, N_{x_4} and N_{x_5}. The spatial step sizes are respectively denoted as Δx_1, Δx_2, Δx_3, Δx_4 and Δx_5. In addition, the number of time nodes and the time step size are respectively denoted as N_t and Δt.

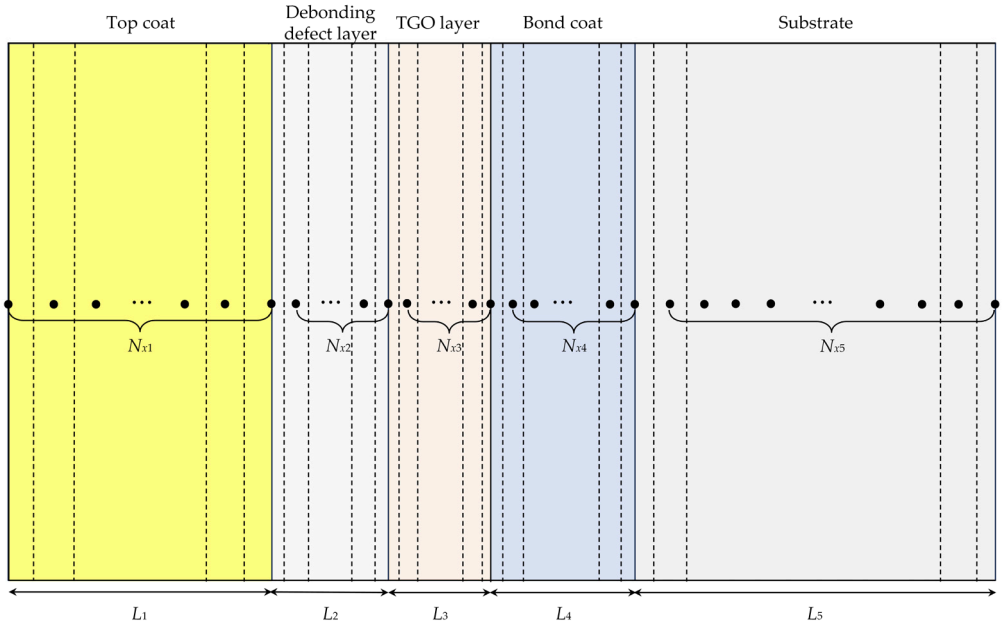


Figure 2. The spatial node distribution and the thickness of the top coat, the debonding defect layer, the TGO layer, the bond coat and the substrate in the forward model.

Based on grid generation, the FVM is employed to discretize Equations (1)–(3), and the following dimensionless parameters are introduced:

$$T_i' = \frac{T_i}{T_{ini}},\ G' = \frac{G}{4n_1^2\sigma T_{ini}^4},\ \Delta x_i' = \frac{\Delta x_i}{L_i},\ \Delta t_i' = \frac{\lambda_i \Delta t}{\rho_i c_i L_i^2},\ N_{\mathrm{cr}} = \frac{\lambda_1 \kappa}{4n_1^2\sigma T_{ini}^3} \tag{15}$$

Accordingly, the dimensionless form of the governing equations can be written as:

$$div\left(\overrightarrow{grad}G'\right) = (1-\omega)3(\kappa L_1)^2\left(G' - T_1'^4\right) \tag{16}$$

$$\frac{\partial T_1'}{\partial t_1'} = div\left(\overrightarrow{grad}T_1'\right) + div\left(\frac{1}{3N_{\mathrm{cr}}}\overrightarrow{grad}G'\right) \tag{17}$$

$$\frac{\partial T_i'}{\partial t_i'} = div\left(\overrightarrow{grad}T_i'\right) \qquad i = 2, 3, 4, 5 \tag{18}$$

The dimensionless boundary conditions can be written as:

$$-\left.\frac{\partial T_1'}{\partial x_1'}\right|_{x_1'=0} - \left.\frac{1}{3N_{\mathrm{cr}}}\frac{\partial G'}{\partial x_1'}\right|_{x_1'=0} = \frac{h_{g1}L_1}{\lambda_1}\left(\frac{T_{g1}}{T_{ini}} - T_1'(x_1'=0)\right) + \frac{\varepsilon_{1\text{-}1}\sigma L_1}{\lambda_1}\left(\frac{T_{g1}^4}{T_{ini}} - T_1'^4(x_1'=0)T_{ini}^3\right) \tag{19}$$

$$\begin{cases} -\left.\frac{\partial T_1'}{\partial x_1'}\right|_{x_1'=1} - \left.\frac{1}{3N_{\mathrm{cr}}}\frac{\partial G'}{\partial x_1'}\right|_{x_1'=1} = -\frac{\lambda_2 L_1}{\lambda_1 L_2}\left.\frac{\partial T_2'}{\partial x_2'}\right|_{x_2'=0} + \frac{L_1}{\lambda_1}\frac{q_r}{T_{ini}} \\ T_1'|_{x_1'=1} = T_2'|_{x_2'=0} \end{cases} \tag{20}$$

$$\begin{cases} -\left.\frac{\partial T_2'}{\partial x_2'}\right|_{x_2'=1} + \frac{L_2}{\lambda_2}\frac{q_r}{T_{ini}} = -\frac{\lambda_3 L_2}{\lambda_2 L_3}\left.\frac{\partial T_3'}{\partial x_3'}\right|_{x_3'=0} \\ T_2'|_{x_2'=1} = T_3'|_{x_3'=0} \end{cases} \tag{21}$$

$$\begin{cases} -\left.\frac{\partial T_3'}{\partial x_3'}\right|_{x_3'=1} = -\frac{\lambda_4 L_3}{\lambda_3 L_4}\left.\frac{\partial T_4'}{\partial x_4'}\right|_{x_4'=0} \\ T_3'|_{x_3'=1} = T_4'|_{x_4'=0} \end{cases} \tag{22}$$

$$\begin{cases} -\frac{\partial T_4'}{\partial x_4'}\Big|_{x_4'=1} = -\frac{\lambda_5 L_4}{\lambda_4 L_5}\frac{\partial T_5'}{\partial x_5'}\Big|_{x_5'=0} \\ T_4'|_{x_4'=1} = T_5'|_{x_5'=0} \end{cases} \tag{23}$$

$$-\frac{\partial T_5'}{\partial x_5'}\Big|_{x_5'=1} = \frac{h_{g5}L_5}{\lambda_5}\left(T_5'(x_5'=1) - \frac{T_{g5}}{T_{ini}}\right) + \frac{\varepsilon_{5\text{-}2}\sigma L_5}{\lambda_5}\left(T_5'^4(x_5'=1)T_{ini}^3 - \frac{T_{g5}^4}{T_{ini}}\right) \tag{24}$$

$$x_1' = 0 : -\frac{2}{3\kappa L_1}\frac{2-\varepsilon_{1\text{-}1}}{\varepsilon_{1\text{-}1}}\frac{\partial G'}{\partial x_1'} + G' = T_1'^4 \tag{25}$$

$$x_1' = 1 : \frac{2}{3\kappa L_1}\frac{2-\varepsilon_{1\text{-}2}}{\varepsilon_{1\text{-}2}}\frac{\partial G'}{\partial x_1'} + G' = T_1'^4 \tag{26}$$

The dimensionless initial conditions can be written as:

$$\forall x_i' : T'(x_i', 0) = 1 \tag{27}$$

$$\forall x_1' : G'(x_1', 0) = 1 \tag{28}$$

The time term in the forward heat transfer model adopts a fully implicit scheme. Within each time step, a synchronous iterative strategy across all layers is employed for the solution. Specifically, for the top coat, in a single iteration, the Thomas algorithm is first applied to separately solve the dimensionless discrete equations with temperature and incident radiation as unknown variables, followed by decoupling via Picard iteration. For all other layers, only the Thomas algorithm is utilized to solve the dimensionless discrete equations with temperature as the sole variable. The convergence criteria for the above iterations are set as follows: the maximum absolute deviation of the temperature field between two successive iterations is less than 10^{-3} K, and the maximum absolute deviation of the radiation field between two successive iterations is less than 10^{-3} W/m^2 (the radiation field criterion applies only to the top coat). Meanwhile, a maximum iteration number of 1000 is set to avoid infinite loops caused by abnormal computational errors.

2.3. Validation of the Forward Model

To ensure the reliability of parameter estimation based on the forward model, the validation of the forward model's grid independence and results accuracy is essential. Given that interface debonding defects usually appear after the thickness of the TGO reaches a certain threshold, the validation of the forward model is performed under two representative scenarios:

Scenario 1: A defect-free configuration of the TBC system involving only the TGO layer (i.e., $L_2 = 0$).

Scenario 2: A defective configuration of the TBC system involving the TGO layer and the debonding defect layer.

In Scenario 1, except that the debonding defect layer thickness (L_2) is zero, the values of all other parameters remain consistent with those in Scenario 2. The parameter values in Scenario 2 are given as follows: the thickness of the top coat is $L_1 = 150$ μm, the refractive index of the top coat is $n_1 = 1.58$, the temperature of the high-temperature gas is $T_{g1} = 2000$ K, and the convective heat transfer coefficient is $h_{g1} = 250$ W/m^2/K [37]. In addition, the thickness of the debonding defect layer, the TGO layer, the bond coat and the substrate are respectively $L_2 = 20$ μm, $L_3 = 10$ μm, $L_4 = 50$ μm, and $L_5 = 1.4$ mm. The temperature of the low-temperature gas is $T_{g5} = 300$ K, the initial temperature is T_{ini} = 300 K, and the convective heat transfer coefficient is $h_{g5} = 110$ W/m^2/K. Furthermore, the formula for N_{cr} given in Equation (15) only serves the purpose of nondimensionalization. When evaluating the relative contribution of conductive and radiative heat transfer within the semi-transparent coating at any given moment, the instantaneous temperature

at that time should be utilized, rather than the initial temperature specified in Equation (15). To reduce the computational complexity and time cost of forward iterative solution and enable feasible dataset construction, simplifications are implemented by assuming constant thermophysical parameters for all layers. The thermophysical parameters of the materials for each layer of the TBC system are shown in Table 1; all thermophysical properties listed are taken from Refs. [37–42].

Table 1. The thermophysical properties of the top coat, the debonding defect layer, the TGO layer, the bond coat and the substrate.

	ρ [kg/m^3]	λ [W/m/K]	c [J/kg/K]	ε	κ_a [m^{-1}]	κ_d [m^{-1}]
Top coat (layer 1)	5600	0.62	625	$\varepsilon_{1\text{-}1} = 0.97$ $\varepsilon_{1\text{-}2} = 0.92$	30	10,000
Debonding defect layer (layer 2)	0.6954	0.0626	1115	—	—	—
TGO layer (layer 3)	3960	21	1330	$\varepsilon_{3\text{-}1} = 0.35$	—	—
Bond coat (layer 4)	6900	17	1370	—	—	—
Substrate (layer 5)	8500	33	500	$\varepsilon_{5\text{-}2} = 0.6$	—	—

2.3.1. Validation of the Forward Model in Scenario 1

For Scenario 1, four grid generation strategies, namely 31-3-10-280 (grid 1), 61-5-20-560 (grid 2), 121-10-40-1120 (grid 3), and 241-20-80-2240 (grid 4), are considered. Given that the simulation time is 30 s and the number of time nodes is $N_t = 6000$, the time-varying temperature fields at the front ($x = 0$) and rear ($x = L$) surfaces of the TBC system under four grid generation strategies are calculated to validate the grid independence. The results are shown in Figure 3.

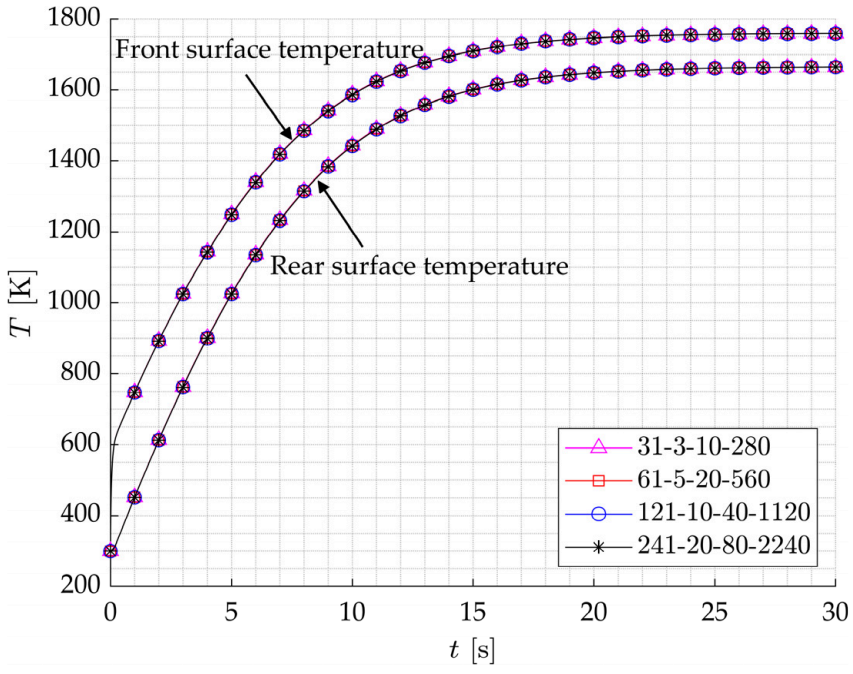


Figure 3. The time-varying temperature fields at the front and rear surfaces of the TBC system in Scenario 1 under four grid generation strategies.

As shown in Figure 3, for both the front and rear surfaces, the temperature field curves under the four grid generation strategies coincide very well. To quantify the effect of grid density on the accuracy of the temperature fields, the relative errors and absolute errors of the front- and rear-surface temperatures under the first three grids are calculated at each time node, relative to those of the fourth grid. The maximum values of both errors are then computed, with results shown in Table 2.

Table 2. The maximum values of the relative and absolute errors for the front- and rear-surface temperatures of the system in Scenario 1 under the first three grids relative to those of the fourth grid at each time node.

	Grid 1 Relative to Grid 4	Grid 2 Relative to Grid 4	Grid 3 Relative to Grid 4
Maximum value of the relative error for $T_{1\text{-}1}$	0.159%	0.092%	0.031%
Maximum value of the relative error for $T_{5\text{-}2}$	0.222%	0.134%	0.045%
Maximum value of the absolute error for $T_{1\text{-}1}$	2.035 K	1.190 K	0.396 K
Maximum value of the absolute error for $T_{5\text{-}2}$	2.391 K	1.441 K	0.480 K

As shown in Table 2, with the increase in grid density, both the maximum relative error and the maximum absolute error of the front- and rear-surface temperatures of the system exhibit a decreasing trend. Compared with the results obtained using grid 4, the maximum relative error of the front- and rear-surface temperatures computed with grid 3 is below 0.05%, and the maximum absolute error is less than 0.5 K, which satisfies the requirements of engineering calculation accuracy. The grid independence of the forward model in Scenario 1 is thus verified. Considering both computational accuracy and efficiency, grid 3 will be selected as the grid for subsequent calculations.

Based on the grid independence validation, the temperature field of the forward model is compared with the simulation results from the finite element commercial software (using a mesh of ~295,000 elements) under the same conditions to validate the accuracy of the forward model. As shown in Figure 4, for the temperature fields at the front and rear surfaces of the system, the results from the forward model based on the FVM-P1 (self-written code) exhibit high consistency with those from the FEM-P1 and FEM-DOM, especially as they approach steady state, where the results of both methods almost perfectly coincide. Slight differences exist between the two methods during the temperature rise phase before reaching steady state. Specifically, at each time step in this phase, taking the time-varying temperatures of the front and rear surfaces of the system as an example, the arithmetic means of the relative errors of the FVM-P1 relative to the FEM-P1 are 0.296% ($T_{1\text{-}1}$) and 0.409% ($T_{5\text{-}2}$), and the maximum values of the relative errors are 1.552% ($T_{1\text{-}1}$) and 0.703% ($T_{5\text{-}2}$). The arithmetic means of the relative errors of the FVM-P1 relative to the FEM-DOM are 0.323% ($T_{1\text{-}1}$) and 0.435% ($T_{5\text{-}2}$), and the maximum values of the relative errors are 1.351% ($T_{1\text{-}1}$) and 0.875% ($T_{5\text{-}2}$). Regarding computational speed, the FVM-P1 takes approximately 1.95 s, while the FEM-P1 and the FEM-DOM respectively take 2078 s and 7907 s. These results effectively validate the applicability and rapidity of the FVM-P1, as well as the accuracy of the forward model in Scenario 1.

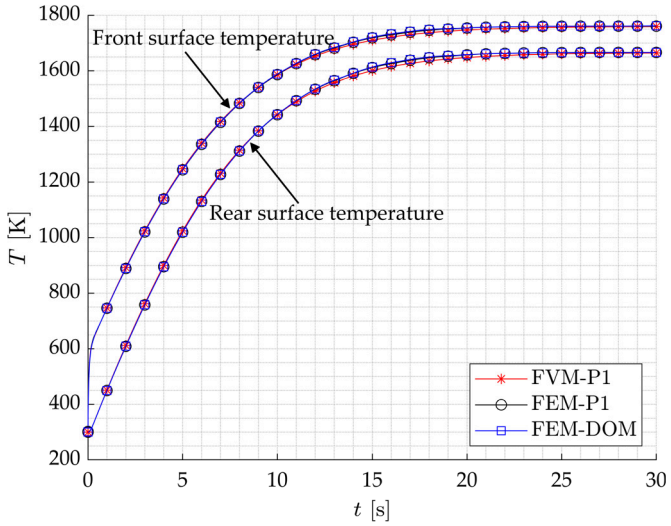


Figure 4. Validation of the front- and rear-surface temperature fields of the forward model in Scenario 1.

2.3.2. Validation of Forward Model in Scenario 2

For Scenario 2, four grid generation strategies are employed, specifically 31-25-3-10-280 (grid 1), 61-50-5-20-560 (grid 2), 121-100-10-40-1120 (grid 3), and 241-200-20-80-2240 (grid 4). The simulation duration and the number of time steps is the same with Scenario 1 (30 s and $N_t = 6000$). The time-varying temperature fields at the front $(x = 0)$ and rear $(x = L)$ surface of the TBC system in Scenario 2 under four grid generation strategies are shown in Figure 5.

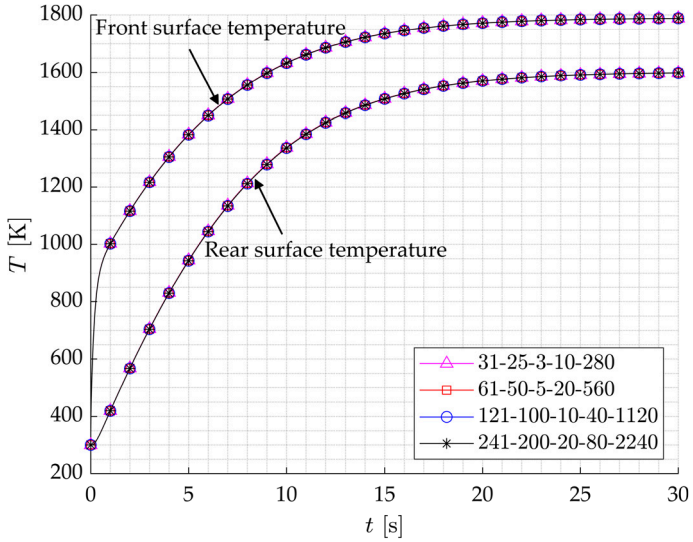


Figure 5. Time-varying temperature fields at the front and rear surfaces of the TBC system in Scenario 2 under four grid generation strategies.

As shown in Figure 5 under four grid generation strategies, the temperature field curves of the system's front surface exhibit very good coincidence, and the same applies to those of the rear surface. Following the same procedure as in Scenario 1, the relative errors and absolute errors of the front- and rear-surface temperatures under the first three grids are calculated at each time node, relative to those of the fourth grid. The maximum values of both errors are then computed, with the results shown in Table 3.

Table 3. The maximum values of the relative and absolute errors for the front- and rear-surface temperatures of the system in Scenario 2 under the first three grids relative to those of the fourth grid at each time node.

Scenario 2	Grid 1 Relative to Grid 4	Grid 2 Relative to Grid 4	Grid 3 Relative to Grid 4
Maximum value of the relative error for $T_{1\text{-}1}$	0.213%	0.091%	0.030%
Maximum value of the relative error for $T_{5\text{-}2}$	0.231%	0.136%	0.045%
Maximum value of the absolute error for $T_{1\text{-}1}$	1.664 K	0.909 K	0.303 K
Maximum value of the absolute error for $T_{5\text{-}2}$	2.223 K	1.340 K	0.446 K

As shown in Table 3, for the front- and rear-surface temperatures of the system, both the relative and absolute errors demonstrate a decreasing trend in their maximum values with the increase in the grid density. Compared with the results from grid 4, the maximum relative error of the front- and rear-surface temperatures obtained using grid 3 is below 0.05%, and the maximum absolute error is less than 0.5 K, verifying the grid independence of the forward model in Scenario 2. Grid 3 is selected as the grid for subsequent calculations. Finally, as shown in Figure 6, based on the grid independence validation, the accuracy of the forward model in Scenario 2 is also well-validated by the FEM. On one hand, similar to Scenario 1, the calculation results based on the FVM and the FEM exhibit nearly perfect agreement in the steady state phase. On the other hand, at each time step during the unsteady phase, taking the time-varying temperatures of the front and rear surfaces of the system as an example, the arithmetic means of the relative errors of the FVM-P1 relative to the FEM-P1 are 0.224% ($T_{1\text{-}1}$) and 0.411% ($T_{5\text{-}2}$), while the maximum values of the relative errors are 2.431% ($T_{1\text{-}1}$) and 1.053% ($T_{5\text{-}2}$). The arithmetic means of the relative errors of the FVM-P1 relative to the FEM-DOM are 0.228% ($T_{1\text{-}1}$) and 0.491% ($T_{5\text{-}2}$), and the maximum values of the relative errors are 1.519% ($T_{1\text{-}1}$) and 0.966% ($T_{5\text{-}2}$). As for computational costs, the FVM-P1 takes approximately 2.33 s, while the FEM-P1 and the FEM-DOM take 3601 s and 11,513 s, respectively. These results also effectively validate the applicability and rapidity of the FVM-P1, as well as its accuracy in Scenario 2.

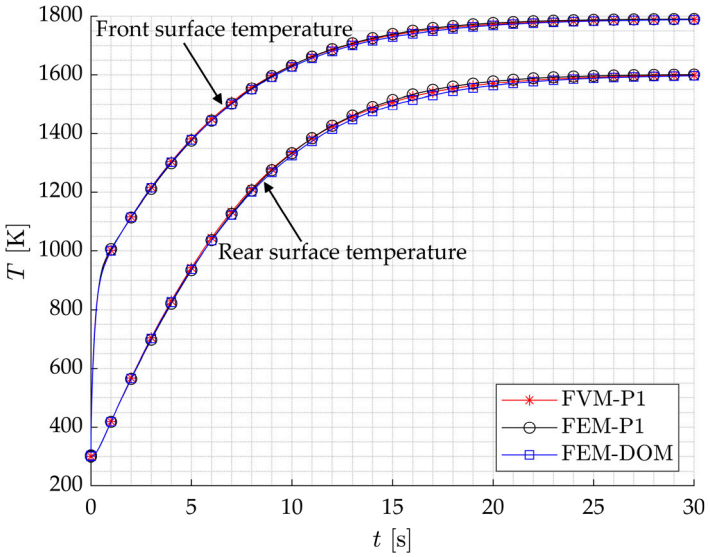


Figure 6. Validation of the front- and rear-surface temperature fields of the forward model in Scenario 2.

3. Sensitivity Study

For parameter estimation problems, sensitivity study is important since it refers to the degree to which system observables respond to variations in parameters, thereby quantifying the relative influence of these parameters on the system's outputs. Through sensitivity study, the optimal estimation range can be found, which helps to improve the estimation efficacy. For the multi-parameter simultaneous estimation problem studied, the front- and rear-surface temperatures of the TBC system (i.e., the external surface temperature $T_{1\text{-}1}$ of the top coat at $x = 0$ and the external surface temperature $T_{5\text{-}2}$ of the substrate at $x = L$) are selected as observables for parameter sensitivity study. The normalized sensitivity of these observables to the top coat thermal conductivity λ_1 ($S_T(\lambda_1)$), the debonding defect layer thickness L_2 ($S_T(L_2)$) and the TGO layer thickness L_3 ($S_T(L_3)$) are defined as follows:

$$S_T(\lambda_1) = \frac{\partial T}{\partial \lambda_1}\frac{\lambda_1}{T}, \quad S_T(L_2) = \frac{\partial T}{\partial L_2}\frac{L_2}{T}, \quad S_T(L_3) = \frac{\partial T}{\partial L_3}\frac{L_3}{T} \tag{29}$$

Next, two estimation cases are considered:

Case 1: a two-parameter simultaneous estimation in Scenario 1.

Case 2: a three-parameter simultaneous estimation in Scenario 2.

Based on the literature review [43,44], with the existing parameter values as references, the target values of parameters to be estimated for different combinations under two cases are selected within reasonable ranges and presented in Table 4.

Table 4. The values of three combinations of the (λ_1, L_3) in Case 1 and those of the (λ_1, L_2, L_3) in Case 2.

Case 1: (λ_1 [W/m/K], L_3 [μm])	Case 2: (λ_1 [W/m/K], L_2 [μm], L_3 [μm])
Combination 1: (1.56, 3.9)	Combination 1: (2.12, 6.3, 7.8)
Combination 2: (0.62, 5.3)	Combination 2: (0.56, 21.5, 10.9)
Combination 3: (1.13, 7.1)	Combination 3: (1.68, 51.3, 12)

3.1. Sensitivity Study in Case 1

With all other input parameters of the forward model (except λ_1 and L_3) set to the same values as those in Scenario 1 of Section 2.3, the normalized sensitivity curves of the front-surface temperature $T_{1\text{-}1}$ and the rear-surface temperature $T_{5\text{-}2}$ with respect to the thermal conductivity of the top coat and the thickness of the TGO layer are shown in Figure 7. As indicated by Figure 7, for the two-parameter simultaneous estimation problem, the order of magnitude of the normalized sensitivity of temperature observables to the thickness of the TGO layer is much smaller than that to the thermal conductivity of the top coat. Specifically, $T_{1\text{-}1}$ exhibits higher sensitivity than $T_{5\text{-}2}$ to the thermal conductivity of the top coat, whereas $T_{5\text{-}2}$ is more sensitive to the thickness of the TGO layer than $T_{1\text{-}1}$. For the estimation interval, it should contain as much information as possible without redundancy, particularly the regions where the sensitivity curves show significant changes. Overall, for the two-parameter simultaneous estimation,$T_{1\text{-}1}$ and $T_{5\text{-}2}$ are selected as observables, with [0, 20 s] chosen as the estimation interval.

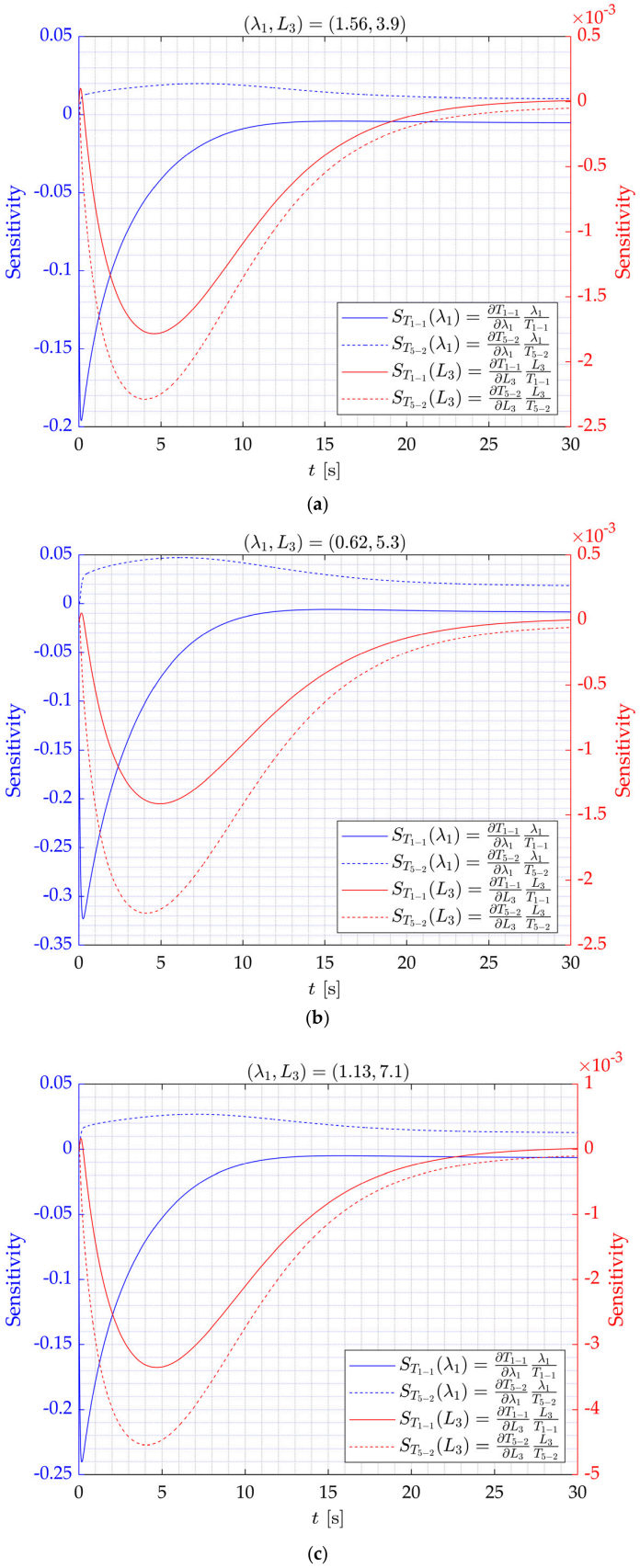


Figure 7. Normalized sensitivity evolution of $T_{1\text{-}1}$ and $T_{5\text{-}2}$ to λ_1 (left axis) and L_3 (right axis) for: (**a**) Combination 1 in Case 1, (**b**) Combination 2 in Case 1, (**c**) Combination 3 in Case 1.

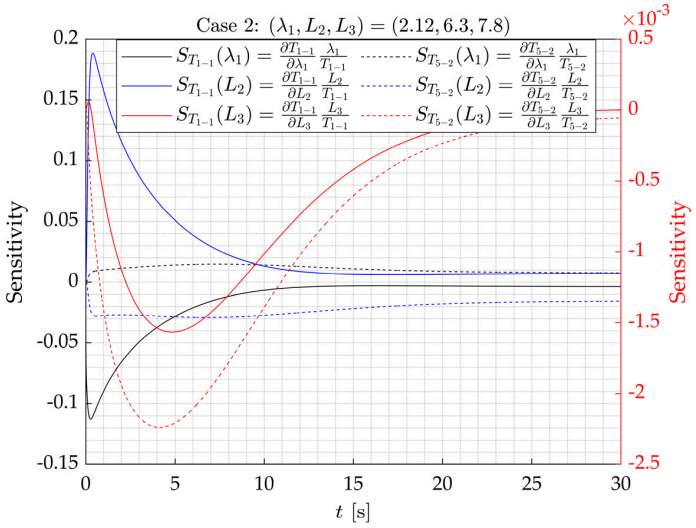
To quantitatively evaluate the linear coupling degree among the normalized sensitivity curves of parameters to be estimated, the Pearson correlation coefficient matrices are respectively calculated under $T_{1\text{-}1}$ and $T_{5\text{-}2}$ with Combinations 1, 2 and 3. The results indicate that: For the two-parameter simultaneous estimation (Case 1), when $T_{5\text{-}2}$ is adopted as the observation, the Pearson correlation coefficients between the normalized sensitivity sequences of top coat thermal conductivity λ_1 and TGO layer thickness L_3 are respectively -0.885, -0.963 and -0.914 for Combinations 1, 2 and 3. These values demonstrate strong linear coupling and severe ill-posedness is prone to occur. In contrast, when $T_{1\text{-}1}$ serves as the observation, the correlation coefficients between the normalized sensitivity sequences of λ_1 and L_3 are only 0.362, 0.312 and 0.352 for Combinations 1, 2 and 3, indicating weak-to-moderate linear coupling. Overall, $T_{1\text{-}1}$ could mitigate mutual interference during parameter estimation and facilitate parameter decoupling. Meanwhile, $T_{5\text{-}2}$ contains abundant thermal response information and provides additional constraints for estimation. The complementary effect of $T_{1\text{-}1}$ and $T_{5\text{-}2}$ during estimation reduces the ill-posedness of the inverse problem and ensures the uniqueness and numerical stability of the solutions.

3.2. Sensitivity Study in Case 2

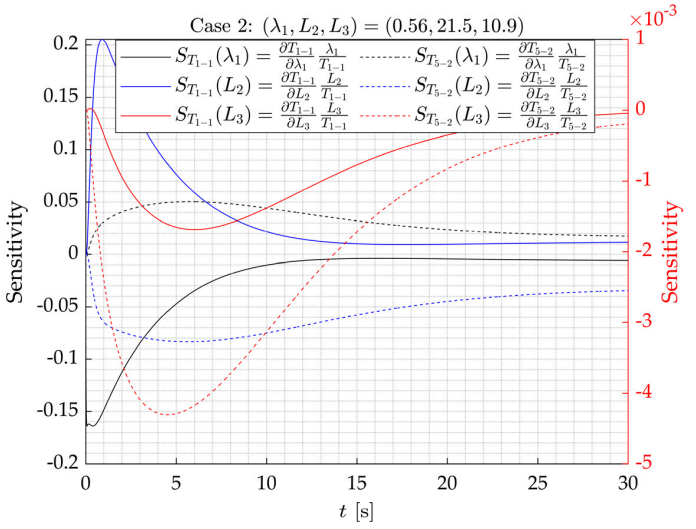
Similar to Case 1, with all other input parameters of the forward model (except λ_1, L_2 and L_3) taking the same values as those in Scenario 2 of Section 2.3, the normalized sensitivity curves of $T_{1\text{-}1}$ and $T_{5\text{-}2}$tothe λ_1, L_2 and L_3 for the three combinations listed in Table 4 are shown in Figure 8.

As indicated by Figure 8, for the three-parameter simultaneous estimation problem, the order of magnitude of the normalized sensitivity of temperature observables to the thickness of the TGO layer is the smallest overall, while that to the thickness of the debonding defect layer is the largest, and the sensitivity to the thermal conductivity of the top coat lies between the two. Individually, $T_{1\text{-}1}$ exhibits higher sensitivity than $T_{5\text{-}2}$ to both the thermal conductivity of the top coat and the thickness of the debonding defect layer, whereas $T_{5\text{-}2}$ is more sensitive to the thickness of the TGO layer than $T_{1\text{-}1}$. Furthermore, the temperature sensitivities of the defect layer thickness and TGO layer thickness in Combination 1 are lower than those in the other two combinations. Considering the smaller values of these two parameters as well as the coupled influence from the variation in thermal conductivity, it can be inferred that the sensitivities of these two parameters decrease with the reduction in their respective values within the parameter range investigated in this study. Consequently, in the subsequent training of the neural network, the training data for the defect layer thickness and TGO layer thickness within a small-scale range will be augmented to improve the estimation accuracy of these two parameters. For the estimation interval, most of the variation information in these sensitivity curves is contained within 20 s. Therefore, for the three-parameter simultaneous estimation, [0, 20 s] is selected as the estimation interval.

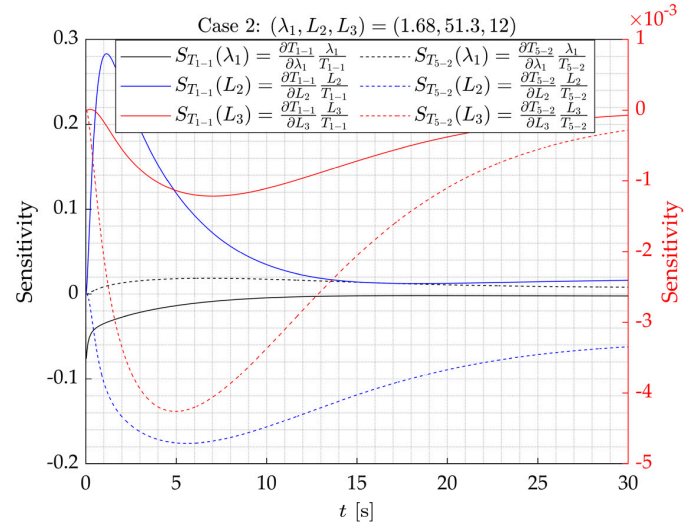
Similarly, the Pearson correlation matrices for three-parameter simultaneous estimation (Case 2) are given below where superscripts 1–3 stand for Combinations 1, 2 and 3. For each matrix, Column 1, 2 and 3 respectively contains correlation coefficients relative to the normalized sensitivity sequences of λ_1, L_2 and L_3.



(**a**)



(**b**)



(**c**)

Figure 8. Normalized sensitivity evolution of $T_{1\text{-}1}$ and $T_{5\text{-}2}$ to λ_1 (left axis), L_2 (left axis) and L_3 (right axis) for: (**a**) Combination 1 in Case 2, (**b**) Combination 2 in Case 2, (**c**) Combination 3 in Case 2.

$$R^1_{T_{1\text{-}1}} = \begin{bmatrix} 1.000 & -0.985 & -0.343 \\ -0.985 & 1.000 & 0.383 \\ -0.343 & 0.383 & 1.000 \end{bmatrix}, R^2_{T_{1\text{-}1}} = \begin{bmatrix} 1.000 & -0.929 & -0.141 \\ -0.929 & 1.000 & 0.280 \\ -0.141 & 0.280 & 1.000 \end{bmatrix}, R^3_{T_{1\text{-}1}} = \begin{bmatrix} 1.000 & -0.828 & 0.013 \\ -0.828 & 1.000 & -0.166 \\ 0.013 & -0.166 & 1.000 \end{bmatrix}$$
$$R^1_{T_{5\text{-}2}} = \begin{bmatrix} 1.000 & -0.934 & -0.868 \\ -0.934 & 1.000 & 0.935 \\ -0.868 & 0.935 & 1.000 \end{bmatrix}, R^2_{T_{5\text{-}2}} = \begin{bmatrix} 1.000 & -0.994 & -0.979 \\ -0.994 & 1.000 & 0.977 \\ -0.979 & 0.977 & 1.000 \end{bmatrix}, R^3_{T_{5\text{-}2}} = \begin{bmatrix} 1.000 & -0.969 & -0.920 \\ -0.969 & 1.000 & 0.984 \\ -0.920 & 0.984 & 1.000 \end{bmatrix} \quad (30)$$

It can be observed from the matrix that with $T_{1\text{-}1}$ as the observation, the normalized sensitivity sequences of λ_1 and L_3 are highly linearly correlated. In contrast, only weak-to-moderate linear correlation exists between the normalized sensitivity sequences of λ_1 and L_2, as well as the sensitivity sequences of L_2 and L_3. When $T_{5\text{-}2}$ is adopted as the observation, the normalized sensitivity sequences of (λ_1, L_2, L_3) show strong linear coupling pairwise.

Similar to Case 1, $T_{1\text{-}1}$ achieves better parameter decoupling during estimation compared with $T_{5\text{-}2}$, whereas $T_{5\text{-}2}$ can supply additional global constraints. Moreover, constructing a joint sensitivity matrix using both $T_{1\text{-}1}$ and $T_{5\text{-}2}$ and performing singular value decomposition of this matrix will increase the minimum singular value and reduce the matrix condition number, directly demonstrating that combining both observations effectively mitigates the ill-posedness of multi-parameter simultaneous estimation.

4. PCA-Optimized ANN-PSO-Based Accelerated Inverse Model

To accelerate the multi-parameter simultaneous estimation process in high-temperature environments, an inverse model combining the PSO algorithm and BP neural network optimized by PCA was developed and evaluated, whose schematic diagram is depicted in Figure 9.

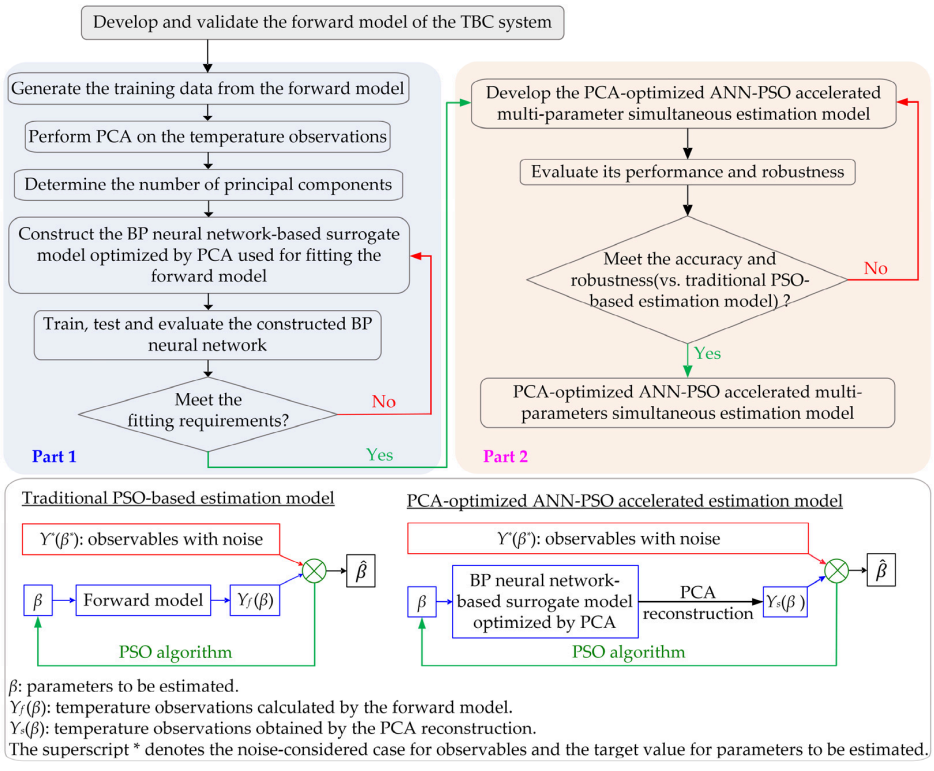


Figure 9. A schematic diagram of the multi-parameter simultaneous estimation model combining a PCA-optimized BP neural network with the PSO algorithm in the inverse method framework.

As shown in Figure 9, the major contents of this section can be decomposed into two parts:

Part 1: Developing a PCA-optimized BP neural network to surrogate the forward model and evaluating its performance.

Part 2: Developing a multi-parameter simultaneous estimation model by combining the above-mentioned surrogate model with the PSO algorithm in the inverse method framework and evaluating its performance.

For Part 1, the general steps are presented as follows:

The surrogate model based on a PCA-optimized BP neural network takes the normalized values of the parameters to be estimated as inputs, and the normalized principal components of the temperature for both the front and rear surfaces as its outputs. Given that the system has a complex heat transfer mechanism, the results of multi-parameter simultaneous estimation exhibit significant errors when the dimension of the observables in the objective function is lower than 2000 within the time range of [0, 20 s]. Without this preprocessing step (PCA), the output dimension of the BP neural network would reach 4000. Constructing and training such a high-dimensional neural network not only consumes substantial computational resources but also leads to suboptimal training performance. Hence, PCA is performed on the temperature to reduce the output dimension of the BP network and streamline its network structure. Specially, the reduction of the output dimension of the BP network based on PCA is divided into two steps:

1. Generate the sample dataset required for PCA.
2. Determine the number of principal components and implement the dimensionality reduction of data.

For the first step, the sample dataset for PCA consists of a front-surface temperature matrix and a rear-surface temperature matrix. Each matrix is composed of a series of temperature vectors of the corresponding surface over the time interval [0, 20 s], and all these vectors are calculated using the forward model. The detailed generation procedure of these temperature matrices is as follows.

For Scenario 1: Each input parameter set for the forward model consists of two categories: variable parameters (thermal conductivity λ_1 of the top coat and thickness L_3 of the TGO layer, which are randomly and uniformly sampled within [0.1, 7.5 W/m/K] and [1, 75 μm], respectively) and the remaining fixed parameters whose values are consistent with those defined in Section 2.3. On this basis, to guarantee the statistical validity and representativeness of the principal components extracted from the front- and rear-surface temperatures, a total of 15,000 input parameters sets are generated and fed into the forward model, yielding 15,000 sets of front-surface temperature vectors and 15,000 sets of rear-surface temperature vectors that constitute the front-surface temperature matrix and the rear-surface temperature matrix for Scenario 1, respectively.

For Scenario 2: Similar to Scenario 1, each input parameter set for the forward model also consists of two categories: variable parameters (thermal conductivity λ_1 of the top coat, thickness L_2 of the defect layer and thickness L_3 of the TGO layer, which are randomly and uniformly sampled within [0.1, 7.5 W/m/K], [0.2, 1000 μm] and [1, 75 μm], respectively) and the remaining fixed parameters with values identical to those specified in Section 2.3. Based on this, 15,000 input parameter sets are firstly generated. Subsequently, an additional 1000 input parameter sets are generated, in which L_2 and L_3 are randomly and uniformly sampled within [0.2, 10 μm] and [1, 10 μm], respectively, while the thermal conductivity λ_1 of the top coat are generated in the same manner as defined above. Thereafter, these 16,000 input parameter sets are fed into the forward model to generate 16,000 front-surface temperature vectors and 16,000 rear-surface temperature vectors, which respectively

form the front-surface temperature matrices and the rear-surface temperature matrices for Scenario 2.

After obtaining the front-surface and rear-surface temperature matrices for both Scenario 1 and Scenario 2, the aforementioned four matrices are standardized and then adopted for the subsequent PCA.

For the second step, the determination of the number of principal components consists of two parts: first, PCA is applied to each standardized temperature matrix separately to obtain the corresponding components matrix in which the number of principal components is determined according to the temperature reconstruction errors calculated from the test temperature matrices. These test temperature matrices are generated in the same manner as before: for each scenario, 500 sets of input parameters are generated within the same ranges as defined previously to obtain the corresponding original front-surface and rear-surface test temperature matrices. Taking the determination of the number of principal components for the front-surface temperature matrix in Scenario 1 as an example: All principal components of this standardized test temperature matrix are first obtained via the PCA mapping relationship established. Subsequently, the first k principal components are selected sequentially (where k takes integer values staring from 1) to reconstruct the test temperature matrix. Then the mean of the sum of the row-wise L_2-norms between the reconstructed matrix and the original matrix is calculated. Finally, the minimum value of k for which this mean is less than 0.1 is taken as the number of principal components for the front-surface temperature in Scenario 1. The same procedure is repeated to obtain the numbers of principal components of other temperature matrices under Scenario 1 and Scenario 2.

For each scenario, the principal components separately extracted from the front- and rear-surface standardized temperature matrices via PCA were concatenated, then normalized and served as the output of the BP neural network, while the parameters to be estimated among the input parameters of the forward model were adopted as the input of the neural network. Specially, for Scenario 1, 2800 sets of (λ_1, L_3) were randomly selected from the 15,000 sets of (λ_1, L_3) aforementioned, and together with their corresponding temperature principal components, constituted the training (80%)–validation (20%) dataset for the BP neural network. In addition, 100 new sets of (λ_1, L_3) and their corresponding temperature principal components were generated to test the generalization ability of this BP neural network (c.f. Figures 10 and 11). For Scenario 2, to improve the fitting accuracy of the BP neural network for cases involving small thicknesses of the defect layer and TGO layer, 3700 sets of (λ_1, L_2, L_3) were first randomly selected from the 16,000 sets of (λ_1, L_2, L_3) aforementioned, where λ_1, L_2 and L_3 were in [0.1, 7.5 W/m/K], [0.2, 1000 μm] and [1, 75 μm], respectively. Then, additional 300 sets of (λ_1, L_2, L_3) were randomly selected from the 1000 sets of (λ_1, L_2, L_3) aforementioned, where λ_1, L_2 and L_3 were in [0.1, 7.5 W/m/K], [0.2, 10 μm] and [1, 10 μm]. These 4000 sets of (λ_1, L_2, L_3), combined with their corresponding temperature principal components, constituted the training (85%)–validation (15%) dataset. Additionally, 100 independent sets of (λ_1, L_2, L_3) and their corresponding temperature principal components were generated to test the generalization ability of the trained BP neural network (c.f. Figures 12 and 13).

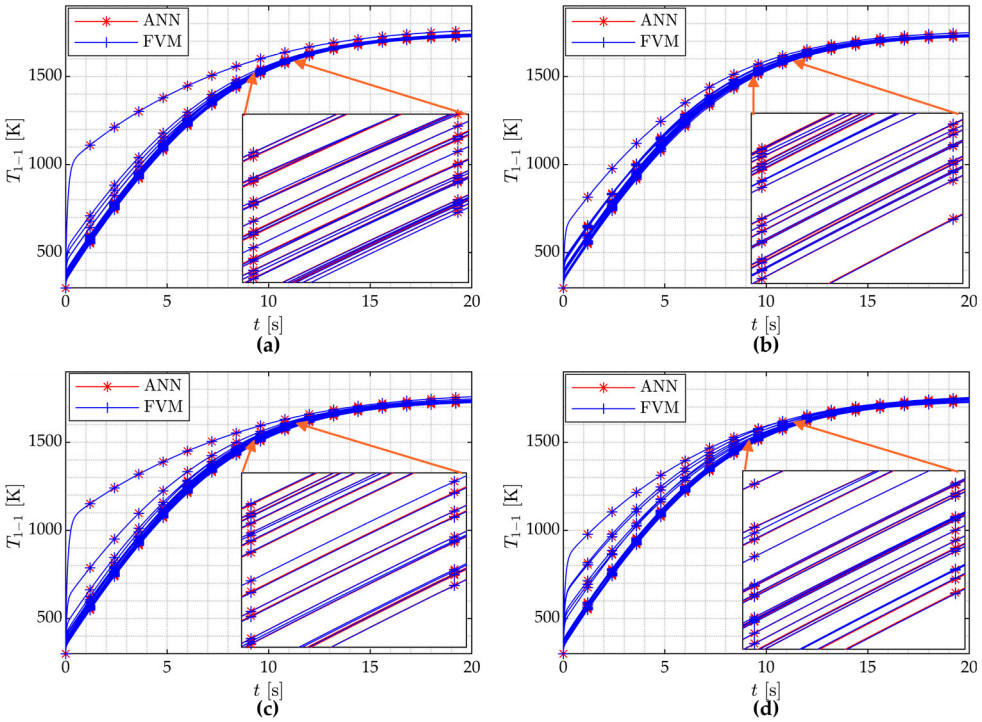


Figure 10. The time-varying front-surface temperature ($T_{1\text{-}1}$) curves of the TBC system in Scenario 1 fitted and reconstructed by the trained BP neural networks in the test phase: (**a**) set 1 to 25 of the test dataset, (**b**) set 26 to 50 of the test dataset, (**c**) set 51 to 75 of the test dataset, (**d**) set 76 to 100 of the test dataset.

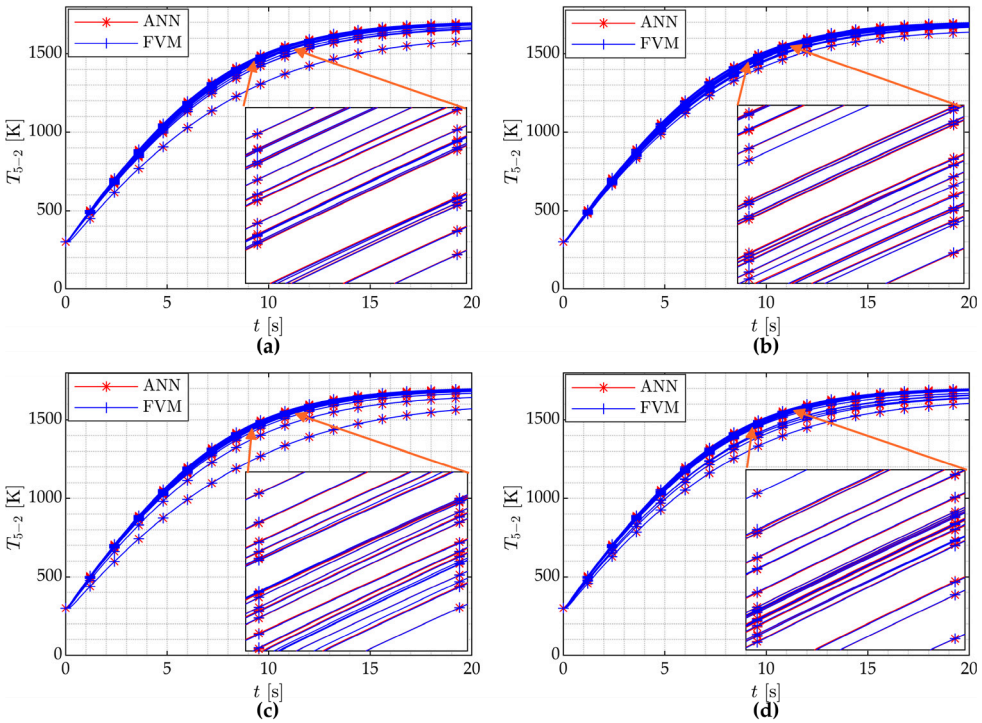


Figure 11. The time-varying rear-surface temperature ($T_{5\text{-}2}$) curves of the TBC system in Scenario 1 fitted and reconstructed by the trained BP neural networks in the test phase: (**a**) set 1 to 25 of the test dataset, (**b**) set 26 to 50 of the test dataset, (**c**) set 51 to 75 of the test dataset, (**d**) set 76 to 100 of the test dataset.

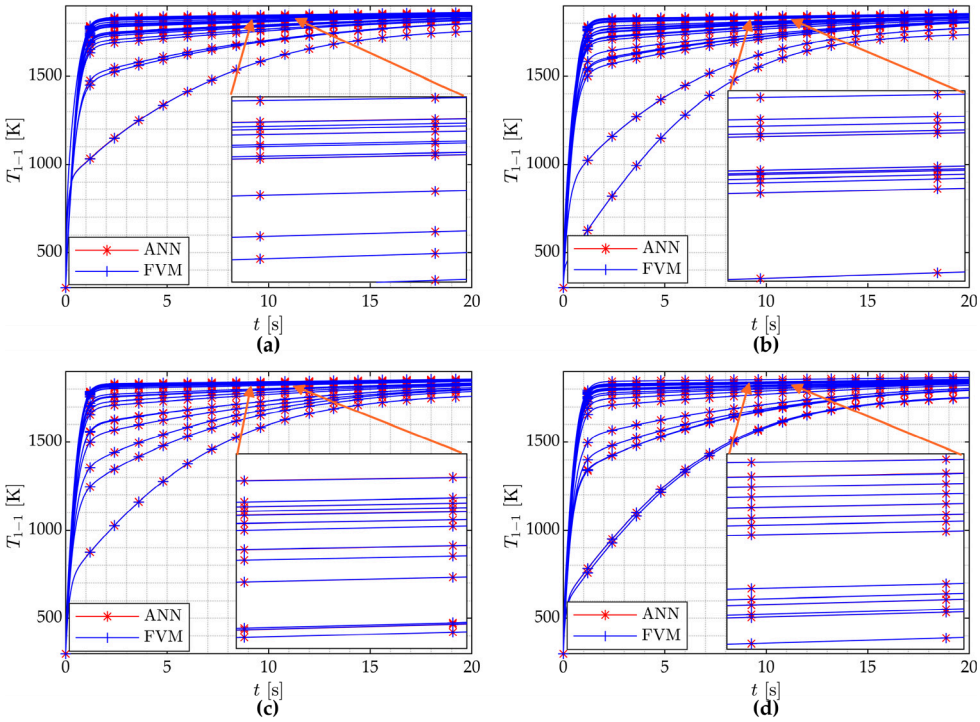


Figure 12. The time-varying front-surface temperature ($T_{1\text{-}1}$) curves of the TBC system in Scenario 2 fitted and reconstructed by the trained BP neural networks in the test phase: (**a**) set 1 to 25 of the test dataset, (**b**) set 26 to 50 of the test dataset, (**c**) set 51 to 75 of the test dataset, (**d**) set 76 to 100 of the test dataset.

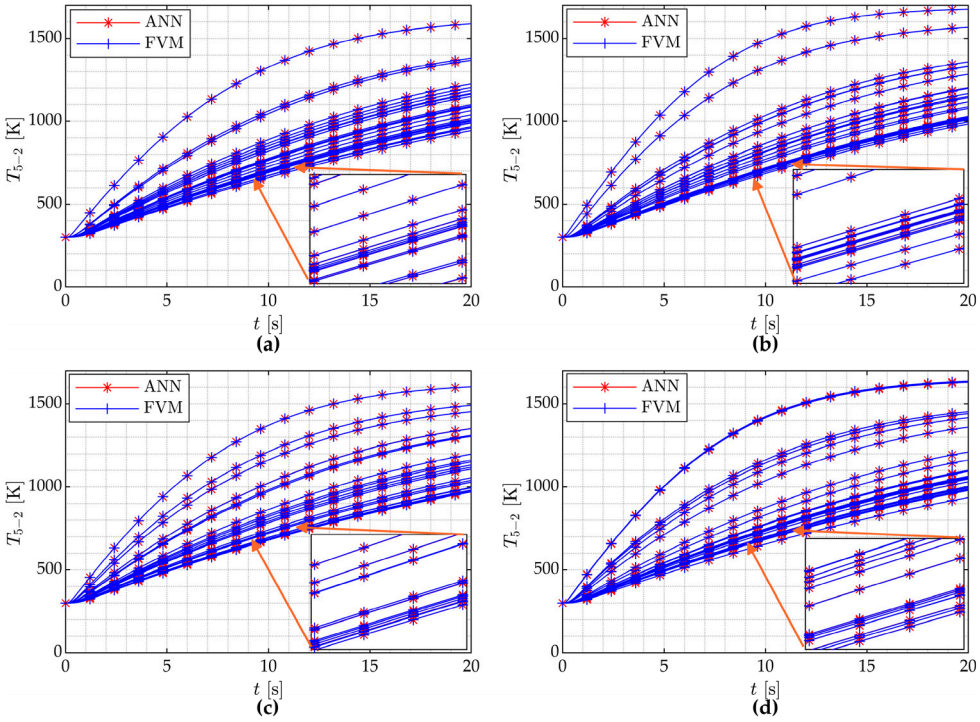


Figure 13. The time-varying rear-surface temperature ($T_{5\text{-}2}$) curves of the TBC system in Scenario 2 fitted and reconstructed by the trained BP neural networks in the test phase: (**a**) set 1 to 25 of the test dataset, (**b**) set 26 to 50 of the test dataset, (**c**) set 51 to 75 of the test dataset, (**d**) set 76 to 100 of the test dataset.

For both scenarios, a three-layer neural network structure was adopted and the Levenberg–Marquardt algorithm was employed as the training function. The hyperbolic

tangent sigmoid function is adopted as the activation function for all hidden layers, while the linear transfer function is used for the output layer. The number of hidden-layer neurons is set to 45 for Scenario 1 and 91 for Scenario 2. The loss function was defined as the mean square error (MSE) between the BP neural network's predicted outputs and the target outputs, and the training process was stopped when the MSE was less than or equal to 1×10^{-6} or the maximum number of training epochs (8000) was reached. The comparisons between the 200 sets (100 sets for Scenario 1 and 100 sets for Scenario 2) of reconstructed temperature fields and the target temperature fields are presented in Figures 10–13. It can be observed that the reconstructed temperature field curves agree excellently with the target ones, which verifies the reliability of the well-trained neural networks. More specifically, for Scenario 1, the maximum mean relative errors between the reconstructed temperature sequences and those obtained from the forward model were 0.011% (front surface) and 0.014% (rear surface), respectively. For Scenario 2, the corresponding maximum mean relative errors were 0.043% (front surface) and 0.067% (rear surface), respectively. These results demonstrate that the well-trained BP neural networks possess exceptionally high predictive precision.

For Part 2, as shown in Figure 9, its main content includes two sections: the development and the evaluation of the PCA-optimized ANN-PSO accelerated inverse model. For the former, the general steps are as follows: the PCA-optimized BP neural network was first employed to substitute the forward model; then, the PSO algorithm was employed to minimize an objective function, formulated as the L_2 norm of the difference between the temperature calculated by the surrogate model and the measured temperatures within the inverse method framework:

$$F_{obj}(\beta) = \|T_{1\text{-}1}(\beta) - T^*_{1\text{-}1}(\beta^*)\|_2 + \|T_{5\text{-}2}(\beta) - T^*_{5\text{-}2}(\beta^*)\|_2 \quad (31)$$

where β is the parameter vector to be estimated, and β^* represents the target value of β. $T_{1\text{-}1}(\beta)$ represents the time-varying front-surface ($x = 0$) temperature reconstructed after surrogate model prediction and $T^*_{1\text{-}1}(\beta^*)$ is the time-varying temperature measurement at the same position in the real system. Similarly, $T_{5\text{-}2}(\beta)$ and $T^*_{5\text{-}2}(\beta^*)$ represent respectively the time-varying rear-surface ($x = L$) temperature reconstructed after surrogate model prediction and the time-varying temperature measurement at the same position in the real system. For the problem studied, random uniform synthetic noise with different intensities was added to the temperature observables $T_{1\text{-}1}(\beta^*)$ and $T_{5\text{-}2}(\beta^*)$ calculated by the forward model. These noise-added observables were used to mimic $T^*_{1\text{-}1}(\beta^*)$ and $T^*_{5\text{-}2}(\beta^*)$ in Formula (17), aiming to simulate the temperatures obtained from actual measurements.

After developing the PCA-optimized ANN-PSO accelerated inverse model, its estimation speed and estimated results were compared with those of the traditional PSO-based inverse model under the same conditions to evaluate its feasibility and efficiency. The detailed results are presented in Section 5.

5. Results and Discussions

In this section, the estimation accuracy and robustness of the PCA-optimized ANN-PSO accelerated inverse model are presented and discussed, in comparison with those of the traditional PSO-based inverse model. All computations were performed on a computer equipped with an Intel Core i7-1165G7 processor (four cores, 2.80 GHz base frequency) and 16 GB of RAM, running the Windows 10 (64-bit) operating system.

5.1. Case 1: Two-Parameter (λ_1, L_3) Simultaneous Estimation

In this case, under the assumption that only a TGO layer exists between the top coat and the bond coat (the debonding defect layer thickness is set as $L_2 = 0$), the simultaneous

estimation of the top coat thermal conductivity λ_1 and the TGO layer thickness L_3 is conducted. Except for λ_1, the thermophysical properties of the top coat, the TGO layer, the bond coat and the substrate are detailed in Table 1. The thickness of the top coat is $L_1 = 150$ μm, with a high-temperature gas of $T_{g1} = 2000$ K on its left side. The bond coat is characterized by a thickness of $L_4 = 50$ μm, while the substrate has a thickness of $L_5 = 1.4$ mm, with a low-temperature gas of $T_{g5} = 300$ K on its right side. The initial temperature of each layer is defined as $T_{ini} = 300$ K. As for the spatial step size, the top coat, the bond coat and the substrate share the same control volume length: 6.25×10^{-7} m for the boundary control volume and 1.25×10^{-6} m for the internal control volume. In addition, the boundary control volume length and the internal control volume length of the TGO layer is 5×10^{-7} m and 1×10^{-6} m, respectively. The total simulation duration for the forward model is 20 s and the time step size is 5×10^{-3} s.

As mentioned above, synthetic noise is added to the temperature observables $T_{1\text{-}1}(\beta^*)$ and $T_{5\text{-}2}(\beta^*)$ to simulate the temperatures $T^*_{1\text{-}1}(\beta^*)$ and $T^*_{5\text{-}2}(\beta^*)$ obtained from actual measurements. Considering that measurement errors increase with temperature rise in practice, a strategy of setting different noise scaling factors for different temperature intervals is adopted to better replicate the measurement error distribution. Specifically, the observables are divided into three temperature intervals: 300–500 K, 500–1000 K, and above 1000 K. When the noise intensity is low, the noise scaling factors I for the three intervals are set to 1/300, 1/200, and 1/100, respectively. When the noise intensity is high, these factors respectively increase to 1/150, 1/100, and 1/50. The noise addition procedure is as follows: For the temperature value of the observables at each time node $T^{(n)}$ ($n \in [1,\ N_t]$), its corresponding temperature interval and the noise scaling factor I are first identified. Next, the corresponding noise range $\pm\, I \cdot T^{(n)}$ is calculated. Thereafter, a random noise value uniformly distributed over this range is generated. Finally, this generated random noise value is added to the original temperature $T^{(n)}$ at each time node, yielding the noisy temperature observable that simulates real-system measured data.

For the key parameters of the PSO algorithm, the number of particles is set to 30 and the maximum number of iterations is 200. Both the individual and social learning factors are set to 1.49. The bounds of the parameters to be estimated are [0.1, 7.5 W/m/K] and [1, 75 μm] for λ_1 and L_3, respectively. For the two-parameter simultaneous estimation, three combinations of the λ_1 and the L_3 are considered, with their target values set to (1.56 W/m/K, 3.9 μm), (0.62 W/m/K, 5.3 μm) and (1.13 W/m/K, 7.1 μm). Under different noise intensities, 20 estimations were performed by the PCA-optimized ANN-PSO accelerated inverse model. The arithmetic means, standard deviations, root mean square errors and average time cost are shown in Table 5.

In terms of estimation accuracy, for the nine cases (three combinations × three noise intensities) presented in Table 5, the maximum relative error of the arithmetic mean (MREAM) of the 20 estimations for the thermal conductivity λ_1 of the top coat obtained by the established PCA-optimized ANN-PSO accelerated inverse model is 0.035%, and the maximum root mean square error (MRMSE) of the 20 estimations for λ_1 is 0.0106 W/m/K. For the TGO layer thickness L_3, the MREAM and the MRMSE of the 20 estimations are respectively 4.245% and 0.719 μm. Furthermore, the estimation accuracy of λ_1 is consistently higher than that of L_3. This distinction is clearly illustrated in the box plots in Figure 14, which is mainly attributed to the higher sensitivity of the former to temperature response, enabling its more accurate identification during the estimation process.

Table 5. Arithmetic mean (AM), standard deviation (SD), root mean square error (RMSE) of (λ_1, L_3) obtained from 20 estimations and average time cost (ATC) per estimation using the PCA-optimized ANN-PSO accelerated inverse model under different noise intensities.

		(λ_1 [W/m/K], L_3 [μm])		
		Combination 1 (1.56, 3.9)	**Combination 2 (0.62, 5.3)**	**Combination 3 (1.13, 7.1)**
Without noise	AM	(1.5599, 4.040)	(0.6200, 5.105)	(1.1301, 7.041)
	SD	(0, 0)	(0, 0)	(0, 0)
	RMSE	(0.0001, 0.140)	(0, 0.195)	(0.0001, 0.059)
	ATC	11.48 s	12.11 s	12.16 s
Low noise intensity	AM	(1.5602, 4.020)	(0.6200, 5.090)	(1.1302, 7.020)
	SD	(0.0054, 0.337)	(0.0010, 0.350)	(0.0030, 0.344)
	RMSE	(0.0053, 0.350)	(0.0010, 0.401)	(0.0029, 0.344)
	ATC	8.53 s	8.87 s	8.54 s
High noise intensity	AM	(1.5604, 4.000)	(0.6201, 5.075)	(1.1304, 7.000)
	SD	(0.0108, 0.674)	(0.0021, 0.700)	(0.0060, 0.687)
	RMSE	(0.0106, 0.665)	(0.0020, 0.719)	(0.0059, 0.677)
	ATC	7.91 s	8.68 s	7.54 s

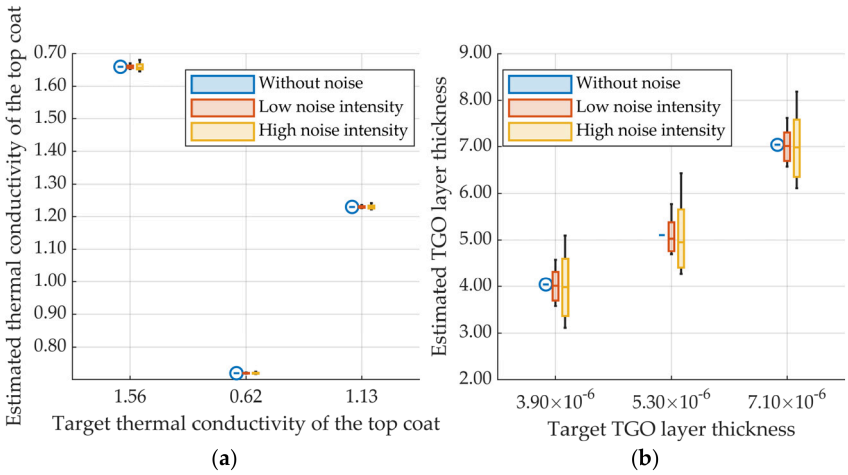


Figure 14. Boxplots of the two-parameter estimation results of the traditional PSO-based inverse model and the PCA-optimized ANN-PSO accelerated inverse model: (**a**) thermal conductivity of the top coat, (**b**) TGO layer thickness.

In terms of the influence of noise intensity on the estimation results, under noise-free conditions, the MREAM of L_3 obtained by both inverse models is non-zero. This error originates from the forward model. Specifically, the forward model is solved using a fixed control volume step size. However, the input TGO layer thickness is not necessarily an integer multiple of the control volume step size, which consequently results in a non-integer number of control volumes. To address this issue, truncation or compensation treatment was applied to the TGO layer thickness, which inevitably results in errors. Such errors are introduced into the training data which is used to train the ANN, and thus the error is ultimately propagated to the PCA-optimized ANN-PSO accelerated inverse model. Moreover, with the increase in noise intensity, both the RMSE and the standard deviation of the 20 estimations for λ_1 and L_3 exhibit an upward trend. This is because higher noise intensities induce more intense deviations of the estimation results from their target values, thereby increasing the dispersion of the 20 estimation results and ultimately leading to an increase in both RMSE and the standard deviation.

As shown in Table 6, these estimation results of the PCA-optimized ANN-PSO accelerated inverse model are of the same order of magnitude as those obtained from the traditional PSO-based inverse model, which are respectively 0.032% (MREAM of λ_1), 0.0072 W/m/K (MRMSE of λ_1), 7.245% (MREAM of L_3) and 0.737 μm (MRMSE of L_3). The above results demonstrate that the PCA-optimized ANN-PSO accelerated inverse model achieves equally excellent accuracy and strong robustness in comparison with the traditional PSO-based inverse model.

Table 6. A comparison of the two-parameter estimation results between the traditional PSO-based inverse model and the PCA-optimized ANN-PSO accelerated inverse model.

	Traditional PSO-Based Inverse Model	**PCA-Optimized ANN-PSO Accelerated Inverse Model**
MREAM of λ_1	0.032%	0.035%
MRMSE of λ_1	0.0072 W/m/K	0.0106 W/m/K
MREAM of L_3	7.245%	4.245%
MRMSE of L_3	0.737 μm	0.719 μm
Average inverse time cost	1240.45 s	9.54 s

As for the estimation speed, the average time cost of the 20 estimations is calculated first for each of the nine cases. These nine values are then averaged to yield the overall average time cost, which decreases from 1240.45 s (traditional PSO-based inverse model) to 9.54 s (PCA-optimized ANN-PSO accelerated inverse model), achieving an average speedup of approximately 130.03 times and realizing a successful balance between accuracy maintenance and significant speed enhancement.

5.2. Case 2: Three-Parameter (λ_1, L_2, L_3) Simultaneous Estimation

Based on Case 1, a debonding defect layer between the top coat and the TGO layer is additionally considered. The control volume length at the boundary of the debonding defect layer is set to 1×10^{-7} m, while that within the debonding defect layer is set to 2×10^{-7} m, with the remaining parameters kept consistent with those in Case 1. At this time, the number of particles in the PSO algorithm is set to 60 and the maximum number of iterations is 300. In addition, both the individual and social learning factors are set to 1.49. The bounds of the parameters to be estimated are [0.1, 7.5 W/m/K], [0.2, 1000 μm] and [1, 75 μm] for λ_1, L_2 and L_3, respectively. For the three-parameter simultaneous estimation, three combinations of λ_1, L_2 and L_3 are considered, with their target values set to (2.12 W/m/K, 6.3 μm, 7.8 μm), (0.56 W/m/K, 21.5 μm, 10.9 μm) and (1.68 W/m/K, 51.3 μm, 12 μm). Under different noise intensities, 20 estimations were performed by the PCA-optimized ANN-PSO accelerated inverse model. The arithmetic means, standard deviations, root mean square errors and average time cost are shown in Table 7.

In terms of estimation accuracy, for all cases presented in Table 7, the MREAM of 20 estimations for λ_1 obtained by the established PCA-optimized ANN-PSO accelerated inverse model is 0.714%, and the MRMSE of the 20 estimations for λ_1 is 0.1831 W/m/K. For the defect layer thickness L_2, the MREAM and MRMSE of the 20 estimations are respectively 1.714% and 0.441 μm. As for L_3, the MREAM and MRMSE of the 20 estimations are individually 2.375% and 1.186 μm.

For the PCA-optimized ANN-PSO accelerated inverse model, under the same noise intensity, the estimation accuracy of the TGO layer thickness is consistently lower than that of the thermal conductivity of the top coat and the defect layer thickness. This trend can be intuitively observed from the box plots in Figure 15. This phenomenon can also be

explained by the significantly lower sensitivity of L_3 to the temperature response relative than those of the other two parameters.

Table 7. Arithmetic mean (AM), standard deviation (SD), root mean square error (RMSE) of (λ_1, L_2, L_3) obtained from 20 estimations and average time cost (ATC) per estimation using the PCA-optimized ANN-PSO accelerated inverse model under different noise intensities.

		(λ_1 [W/m/K], L_2 [μm], L_3 [μm])		
		Combination 1 (2.12, 6.3, 7.8)	**Combination 2 (0.56, 21.5, 10.9)**	**Combination 3 (1.68, 51.3, 12)**
Without noise	AM	(2.1205, 6.206, 7.964)	(0.5604, 21.748, 10.999)	(1.6756, 51.197, 12.238)
	SD	(0, 0, 0)	(0.0010, 0.028, 0.063)	(0.0101, 0.036, 0.054)
	RMSE	(0.0005, 0.094, 0.164)	(0.0010, 0.250, 0.117)	(0.0108, 0.109, 0.243)
	ATC	75.22 s	48.38 s	46.15 s
Low noise intensity	AM	(2.1244, 6.205, 7.943)	(0.5609, 21.757, 10.961)	(1.6729, 51.180, 12.262)
	SD	(0.0947, 0.220, 0.385)	(0.0048, 0.159, 0.489)	(0.0211, 0.120, 0.585)
	RMSE	(0.0924, 0.234, 0.401)	(0.0047, 0.300, 0.481)	(0.0218, 0.167, 0.627)
	ATC	48.83 s	37.03 s	49.08 s
High noise intensity	AM	(2.1299, 6.192, 7.929)	(0.5613, 21.762, 10.959)	(1.6680, 51.151, 12.285)
	SD	(0.1876, 0.439, 0.769)	(0.0090, 0.305, 0.956)	(0.0423, 0.242, 1.181)
	RMSE	(0.1831, 0.441, 0.761)	(0.0089, 0.396, 0.933)	(0.0429, 0.279, 1.186)
	ATC	41.13 s	39.39 s	54.27 s

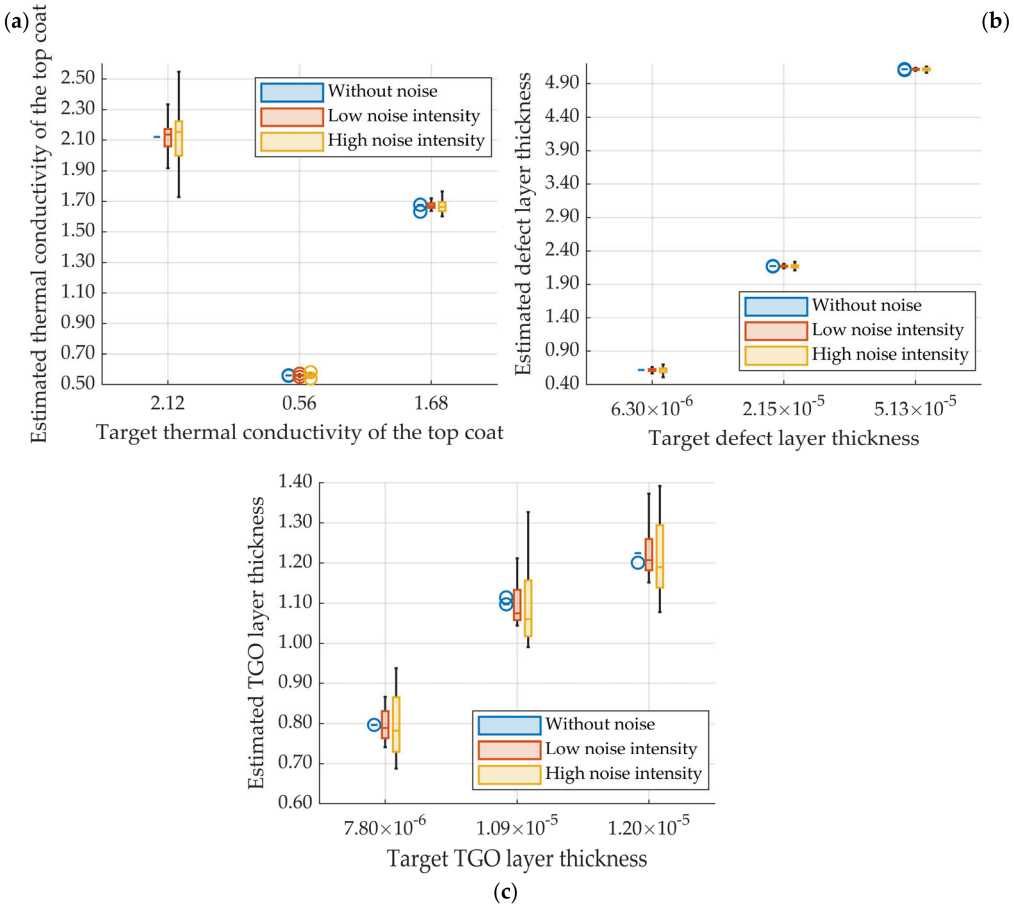


Figure 15. Boxplots of the two-parameter estimation results of the traditional PSO-based inverse model and the PCA-optimized ANN-PSO accelerated inverse model: (**a**) thermal conductivity of the top coat, (**b**) defect layer thickness, (**c**) TGO layer thickness.

Furthermore, for both Combination 1 and Combination 2, the relative errors of the mean of the 20 estimations for λ_1 are smaller than those of L_2 under different noise intensities, whereas Combination 3 shows the opposite trend. From the perspective of sensitivity, for Combination 1 and Combination 2, although the sensitivities of λ_1 and L_2 are of the same order of magnitude, L_2 is affected by truncation or compensation errors in the same way as L_3. Therefore, the estimation accuracy of L_2 is lower than that of λ_1. However, for Combination 3, the order of magnitude of the sensitivity of L_2 is significantly higher than that of λ_1, leading to a higher final estimation accuracy for L_2 relative to that for λ_1.

As shown in Table 8, these estimation results of the PCA-optimized ANN-PSO accelerated inverse model are on the same order of magnitude as those obtained from the traditional PSO-based inverse model, which are respectively 4.090% (MREAM of λ_1), 0.2104 W/m/K (MRMSE of λ_1), 1.937% (MREAM of L_2), 0.373 μm (MRMSE of L_2), 1.487% (MREAM of L_3) and 0.988 μm (MRMSE of L_3). This further validates that the PCA-optimized ANN-PSO accelerated inverse model possesses comparable accuracy and strong robustness relative to the traditional one.

Table 8. A comparison of the three-parameter estimation results between the traditional PSO-based inverse model and the PCA-optimized ANN-PSO accelerated inverse model.

	Traditional PSO-Based Inverse Model	**PCA-Optimized ANN-PSO Accelerated Inverse Model**
MREAM of λ_1	4.090%	0.714%
MRMSE of λ_1	0.2104 W/m/K	0.1831 W/m/K
MREAM of L_2	1.937%	1.714%
MRMSE of L_2	0.373 μm	0.441 μm
MREAM of L_3	1.487%	2.375%
MRMSE of L_3	0.988 μm	1.186 μm
Average inverse time cost	5432.76 s	48.83 s

In terms of estimation speed, the overall average time cost, calculated in the same manner as Case 1, decreases from 5432.7 s (traditional PSO-based inverse model) to 48.83 s (PCA-optimized ANN-PSO accelerated inverse model), achieving an average speedup of approximately 111.26 times.

6. Conclusions and Perspectives

In this study, a novel inverse mathematical model integrating conduction–radiation coupled heat transfer, neural networks, model order reduction and optimization algorithms was developed and applied to the fast and simultaneous estimation of thermophysical properties (the thermal conductivity of the top coat) and geometric parameters (the debonding defect layer thickness and the TGO layer thickness) for TBC systems in high-temperature environments with measurement noise.

First, in terms of the forward heat transfer simulation, a one-dimensional unsteady coupled heat transfer model of the TBC system in high-temperature environments was innovatively developed. Then, this model was fitted and replaced by the PCA-optimized BP neural network to accelerate the simulation process. Subsequently, a multi-parameter simultaneous estimation model combining the above-mentioned neural network with the PSO algorithm in the inverse method framework was developed. Finally, two cases which are respectively the simultaneous estimation of the top coat thermal conductivity and the TGO layer thickness (Case 1) and the simultaneous estimation of the top coat thermal conductivity, the thickness of the debonding defect layer and that of the TGO layer (Case 2) were conducted under noise-free, low noise intensity and high noise intensity conditions.

For Case 1, the maximum relative errors of the arithmetic mean obtained from 20 estimations by the PCA-optimized ANN-PSO accelerated inverse model, under different noise intensity, were 0.035% (for the top coat thermal conductivity) and 4.245% (for the TGO layer thickness), which are of the same order of magnitude as those obtained by the traditional PSO-based inverse model, but achieving an average speedup of approximately 130.03 times relative to the traditional one (from 1240.45 s to 9.54 s). As for Case 2, the maximum relative errors of the arithmetic mean obtained from 20 estimations by the accelerated inverse model under the above noise conditions were 0.714% (for the top coat thermal conductivity), 1.714% (for the defect layer thickness) and 2.375% (for the TGO layer thickness), which are of the same order of magnitude in precision as the results obtained from the traditional inverse model. As for the estimation speed, the accelerated inverse model reduced the overall average time cost from 5432.7 s (traditional PSO-based inverse model) to 48.83 s, achieving an average speedup of approximately 111.26 times.

Furthermore, to address the problems of overlarge neural network scale and high training difficulty arising from the high complexity of the system, this paper proposed a strategy for reducing the scale of artificial neural networks based on the principal component analysis. The results show that this strategy can significantly improve the estimation speed while maintaining nearly identical estimation accuracy, which not only provides a valuable reference for the research on fast and simultaneous estimation of multi-type parameters of complex systems typified by TBC systems, but also demonstrates great potential value in future engineering applications.

Finally, limited by current experimental conditions, the primary work of this study focuses on the theoretical and numerical aspects to demonstrate the feasibility of fast and simultaneous estimation of thermophysical and geometric parameters of TBC systems under high-temperature environments and test the robustness of the inverse model via artificial random noise. Experimental validations will be carried out in future research from the following stages:

1. Fabricate TBC specimens and build a high-temperature thermal cycle shock test bench.
2. Conduct thermal cycle shock experiments under realistic service conditions.
3. Evaluate, revise and optimize the multi-layer coupled heat transfer model for TBC systems based on experimental data. Further investigation into the effects of model dimension, temperature-dependent thermophysical parameters, and irregular morphologies of defects and TGO layers on model accuracy will be carried out where warranted by experimental results.
4. Estimate the thermophysical and geometric parameters of TBC systems using experimental data obtained from thermal cycle shock tests to evaluate the prediction capacity of the inverse model for practical TBC systems. Further investigation into the effects of temperature measurement noise and uncertainties in boundary conditions on estimation accuracy will be carried out to continuously improve estimation accuracy and robustness.

Author Contributions: Conceptualization, Y.L.; methodology, Y.L. and Q.L.; software, Y.L. and Q.L.; validation, Q.L., D.S. and D.L.; formal analysis, Y.L. and Q.L.; investigation, Q.L.; resources, Y.L., D.S. and D.L.; data curation, Y.L. and Q.L.; writing—original draft preparation, Y.L. and Q.L.; writing—review and editing, Y.L., D.S. and D.L.; visualization, Q.L.; supervision, Y.L., D.S. and D.L.; project administration, Y.L.; funding acquisition, Y.L. All authors have read and agreed to the published version of the manuscript.

Funding: This work was supported by Joint Funds of the Natural Science Foundation of Tianjin (No.23JCQNJC00250) and the Tianjin Municipal Education Commission Scientific Research Program Projects (Natural Science) (No.2024KJ101).

Institutional Review Board Statement: Not applicable.

Informed Consent Statement: Not applicable.

Data Availability Statement: The data presented in this study are available on request from the corresponding author.

Conflicts of Interest: The authors declare no conflicts of interest.

Abbreviations

The following abbreviations are used in this manuscript:

ANN	Artificial Neural Network
DOM	Discrete Ordinate Method
FEM	Finite Element Method
FVM	Finite Volume Method
NDT	Non-Destructive Testing
TBC	Thermal Barrier Coating
TGO	Thermally Grown Oxide
PCA	Principal Component Analysis
PSO	Particle Swarm Optimization

Nomenclature

The following nomenclature are used in this manuscript:

c_i	specific heat capacity of the i^{th} layer, J/kg/K
G	incident radiation, W/m^2
G'	dimensionless incident radiation, $G' = G/\left(4n_1^2\sigma T_{ini}^4\right)$
h_{g1}, h_{g5}	convective heat transfer coefficient at the front and rear surface, W/m^2/K
I	noise scaling factor
L_i	thickness of the i^{th} layer, m
L	total thickness of the TBC system ($L = L_1 + L_2 + L_3 + L_4 + L_5$), m
N_t	total number of time nodes
N_{xi}	number of spatial nodes of the i^{th} layer
n_1	refractive index of the top coat
T	temperature, K
TBC	thermal barrier coating
$T^{(n)}$	temperature value of the observables at each time node, K
T'	dimensionless temperature, $T' = T/T_{ini}$
$T_{\text{1-1}}$, $T_{\text{5-2}}$	temperature at the front ($x = 0$) and rear ($x = L$) surfaces, K
T_{g1}, T_{g5}	gas temperature for convection and radiation at $x = 0$ and $x = L$, K
T_i	temperature of the i^{th} layer, K
T_{ini}	initial temperature, K
q_r	radiative heat flux between the boundary of the top coat at $x = L_1$ and the boundary of the TGO layer at $x = L_1 + L_2$, W/m^2
S_T	reduced sensitivity of the surface temperature T to parameters to be estimated
β	parameter to be estimated
β^*	target value of the parameter β to be estimated
Δx_i	spatial step size of the i^{th} layer, m
$\Delta x_i'$	dimensionless spatial step size of the i^{th} layer, $\Delta x_i' = \Delta x_i/L_i$
Δt	time step size, s
$\Delta t'$	dimensionless time step size, $\Delta t' = \lambda_i \Delta t/\left(\rho_i c_i L_i^2\right)$

$\varepsilon_{1\text{-}1}$	emissivity of the left boundary of the top coat ($x = 0$)
$\varepsilon_{1\text{-}2}$	emissivity of the right boundary of the top coat ($x = L_1$)
$\varepsilon_{3\text{-}1}$	emissivity of the left boundary of the TGO layer ($x = L_1 + L_2$)
$\varepsilon_{5\text{-}2}$	emissivity of the right boundary of the substrate layer ($x = L$)
κ_a, κ_d, κ	absorption coefficient, scattering coefficient and extinction coefficient, m^{-1}
λ_i	thermal conductivity of the i^{th} layer, W/m/K
ω	scattering albedo
ρ_i	density of the i^{th} layer, kg/m^3
σ	Stefan–Boltzmann constant
Subscripts	
i	layer index
r	relative to radiation
T	relative to temperature
1-1, 1-2	relative to the front and rear surfaces of the first layer
3-1	relative to the front surface of the third layer
5-2	relative to the rear surface of the fifth layer
Subscripts	
$'$	normalized parameter
$*$	target value
(n)	relative to time node

References

1. Zhang, Z.H.; Huang, Y.; Zhong, S.C.; Lin, T.L.; Zhong, Y.J.; Zeng, Q.M.; Nsengiyumva, W.; Yu, Y.J.; Peng, Z.K. Time of flight improved thermally grown oxide thickness measurement with terahertz spectroscopy. *Front. Mech. Eng.* **2022**, *17*, 49. [CrossRef]
2. Zhu, W.; Zhang, C.X.; Yang, L.; Zhou, Y.C.; Liu, Z.Y. Real-time detection of damage evolution and fracture of EB-PVD thermal barrier coatings under thermal shock: An acoustic emission combined with digital image correlation method. *Surf. Coat. Technol.* **2020**, *399*, 126151. [CrossRef]
3. Kishore, M.B.; Lee, H.G.; Abera, A.G.; Kim, H.J.; Seok, C.S.; Song, S.J. Quantitative evaluation of partial delamination in thermal barrier coatings using ultrasonic C-scan imaging. *Int. J. Precis. Eng. Manuf.* **2020**, *21*, 157–165.
4. Biju, N.; Ganesan, N.; Krishnamurthy, C.V.; Balasubramaniam, K. Defect Sizing Simulation Studies for the Tone-Burst Eddy Current Thermography Using Genetic Algorithm Based Inversion. *J. Nondestruct. Eval.* **2012**, *31*, 342–348. [CrossRef]
5. Roth, D.J.; Reyes-Rodriguez, S.; Zimdars, D.A.; Rauser, R.W.; Ussery, W.W. Terahertz computed tomography of NASA thermal protection system materials. *AIP Conf. Proc.* **2012**, *1430*, 566–572. [CrossRef]
6. Isern, L.; Waddie, A.J.; Chalk, C.; Moore, A.J.; Nicholls, J.R. Non-destructive thickness measurement of thermal barrier coatings using terahertz radiation. *Emergent Mater.* **2021**, *4*, 1547–1557. [CrossRef]
7. Zhu, J.G.; Mao, Z.Z.; Wu, D.L.; Zhou, J.F.; Jiao, D.C.; Shi, W.X.; Zhu, W.Y.; Liu, Z.W. Progress and Trends in Non-destructive Testing for Thermal Barrier Coating Based on Infrared Thermography: A review. *J. Nondestruct. Eval.* **2022**, *41*, 49. [CrossRef]
8. Ptaszek, G.; Cawley, P.; Almond, D.; Pickering, S. Artificial disbonds for calibration of transient thermography inspection of thermal barrier coating systems. *NDT E Int.* **2012**, *45*, 71–78. [CrossRef]
9. Maillet, D.; Andre, S.; Batsale, J.C.; Degiovanni, A.; Moyne, C. *Thermal Quadrupoles: Solving the Heat Equation Through Integral Transforms*, 1st ed.; Wiley: New York, NY, USA, 2000; pp. 311–319.
10. Salazar, A.; Fuente, R.; Mendioroz, A.; Apiñaniz, E.; Celorrio, R. Application of the Thermal Quadrupoles Method to Semitransparent Solids. *Int. J. Thermophys.* **2012**, *33*, 1887–1891. [CrossRef]
11. Wei, L.Y.; Qi, H.; Niu, Z.T.; Ren, Y.T.; Ruan, L.M. Reverse Monte Carlo coupled with Runge-Kutta ray tracing method for radiative heat transfer in graded-index media. *Infrared Phys. Technol.* **2019**, *99*, 5–13. [CrossRef]
12. Fan, C.; Li, X.L.; Xia, X.L.; Sun, C. An unstructured Monte Carlo ray-tracing method for solving radiative heat transfer in 3D gray semitransparent medium. *J. Quant. Spectrosc. Radiat. Transf.* **2019**, *225*, 110–118. [CrossRef]
13. Sans, M.; Farges, O.; Schick, V.; Parent, G. Solving transient coupled conductive and radiative transfers in porous media with a Monte Carlo Method: Characterization of thermal conductivity of foams using a numerical Flash Method. *Int. J. Therm. Sci.* **2022**, *179*, 107656. [CrossRef]
14. Dehghanian, A.; Hosseini Sarvari, S.M. Transient radiative transfer in variable index media using the discrete transfer method. *J. Quant. Spectrosc. Radiat. Transf.* **2020**, *255*, 107259. [CrossRef]

15. Zhang, B.; Xu, C.L.; Wang, S.M. Generalized source Finite Volume Method for radiative transfer equation in participating media. *J. Quant. Spectrosc. Radiat. Transf.* **2017**, *189*, 189–197. [CrossRef]
16. Wang, C.H.; Feng, Y.Y.; Yue, K.; Zhang, X.X. Discontinuous finite element method for combined radiation-conduction heat transfer in participating media. *Int. Commun. Heat Mass Transf.* **2019**, *108*, 104287. [CrossRef]
17. Zhou, R.R.; Li, B.W. The modified discrete ordinates method for radiative heat transfer in two-dimensional cylindrical medium. *Int. J. Heat Mass Transf.* **2019**, *139*, 1018–1030. [CrossRef]
18. Liu, Y.; Billaud, Y.; Saury, D.; Lemonnier, D. Simultaneous identification of thermophysical properties of semitransparent media using an artificial neural network trained by a 2-D axisymmetric direct model. *Numer. Heat Transf. Part A* **2020**, *77*, 890–912. [CrossRef]
19. Girault, M.; Liu, Y.; Billaud, Y.; Benselama, A.M.; Saury, D.; Lemonnier, D. Reduced Order Models for conduction and radiation inside semi-transparent media via the Modal Identification Method. *Int. J. Heat Mass Transf.* **2021**, *168*, 120598. [CrossRef]
20. Sun, J.G. Pulsed Thermal Imaging Measurement of Thermal Properties for Thermal Barrier Coatings Based on a Multilayer Heat Transfer Model. *J. Heat Transf.* **2014**, *136*, 081601. [CrossRef]
21. Zhu, W.; Wang, J.W.; Yang, L.; Zhou, Y.C.; Wei, Y.G.; Wu, R.T. Modeling and simulation of the temperature and stress fields in a 3D turbine blade coated with thermal barrier coatings. *Surf. Coat. Technol.* **2017**, *315*, 443–453. [CrossRef]
22. Tang, Q.J.; Liu, J.Y.; Dai, J.M.; Yu, Z.Y. Theoretical and experimental study on thermal barrier coating (TBC) uneven thickness detection using pulsed infrared thermography technology. *Appl. Therm. Eng.* **2017**, *114*, 770–775. [CrossRef]
23. Adamczyk, W.P.; Kruczek, T.; Moskal, G.; Białecki, R.A. Nondestructive technique of measuring heat conductivity of thermal barrier coatings. *Int. J. Heat Mass Transf.* **2017**, *111*, 442–450. [CrossRef]
24. Gao, C.; Liu, Y.; You, R.Q.; Li, H.W. Theoretical and Numerical Study on Thermal Insulation Performance of Thermal Barrier Coatings. *Energies* **2022**, *15*, 6880. [CrossRef]
25. Yang, X.; Wang, X.Y.; Fang, W.; Hu, G.B.; Liu, Y.T.; Tao, N.; Zhang, C.L. Pulsed thermography with laser beam homogenizing for thickness prediction of thin semi-transparent thermal barrier coatings. *Opt. Lasers Eng.* **2022**, *158*, 107182. [CrossRef]
26. Vavilov, V.P.; Świderski, W. The effects of the partial optical transparency of composites on the results of active thermal testing. *Russ. J. Nondestruct. Test.* **2011**, *47*, 719–723. [CrossRef]
27. Tang, Q.J.; Liu, J.Y.; Wang, Y.; Liu, Y.; Mei, C. Infrared image edge recognition and defect quantitative determination based on the algorithm of fuzzy C-means clustering and Canny operator. *Infrared Laser Eng.* **2016**, *45*, 274–278. [CrossRef]
28. Tang, Q.J.; Dai, J.M.; Liu, J.Y.; Liu, C.S.; Liu, Y.L.; Ren, C.P. Quantitative detection of defects based on Markov–PCA–BP algorithm using pulsed infrared thermography technology. *Infrared Phys. Technol.* **2016**, *77*, 144–148. [CrossRef]
29. Yousefi, B.; Sfarra, S.; Castanedo, C.I.; Maldague, X.P.V. Comparative analysis on thermal non-destructive testing imagery applying Candid Covariance-Free Incremental Principal Component Thermography (CCIPCT). *Infrared Phys. Technol.* **2017**, *85*, 163–169. [CrossRef]
30. Luo, Q.; Gao, B.; Woo, W.L.; Yang, Y. Temporal and spatial deep learning network for infrared thermal defect detection. *NDT E Int.* **2019**, *108*, 102164. [CrossRef]
31. Luo, M.T.; Zhong, S.C.; Yao, L.; Tu, W.L.; Nsengiyumva, W.; Chen, W.Q. Thin thermally grown oxide thickness detection in thermal barrier coatings based on SWT-BP neural network algorithm and terahertz technology. *Appl. Opt.* **2020**, *59*, 4097–4104. [CrossRef] [PubMed]
32. Ye, D.D.; Wang, W.Z.; Zhou, H.T.; Fang, H.J.; Huang, J.B.; Li, Y.J.; Gong, H.H.; Li, Z. Characterization of thermal barrier coatings microstructural features using terahertz spectroscopy. *Surf. Coat. Technol.* **2020**, *394*, 125836. [CrossRef]
33. Shi, L.C.; Long, Y.; Wang, Y.Z.; Chen, X.H.; Zhao, Q.F. Online nondestructive evaluation of TBC crack using infrared thermography. *Meas. Sci. Technol.* **2021**, *32*, 115008. [CrossRef]
34. Shi, L.C.; Long, Y.; Wang, Y.Z.; Chen, X.H.; Zhao, Q.F. Evaluation of internal cracks in turbine blade thermal barrier coating using enhanced multi-scale faster R-CNN model. *Appl. Sci.* **2022**, *12*, 6446. [CrossRef]
35. Jaeger, B.E.; Schmid, S.; Grosse, C.U.; Gögelein, A.; Elischberger, F. Infrared Thermal Imaging-Based Turbine Blade Crack Classification Using Deep Learning. *J. Nondestruct. Eval.* **2022**, *41*, 74. [CrossRef]
36. Modest, M.F. *Radiative Heat Transfer*, 3rd ed.; Academic Press: San Diego, CA, USA, 2013; pp. 502–506.
37. Siegel, R. Internal radiation effects in zirconia thermal barrier coatings. *J. Thermophys. Heat Transf.* **1996**, *10*, 707–709. [CrossRef]
38. Yang, F.; Zhao, X.F.; Xiao, P. Thermal conductivities of YSZ/Al_2O_3 composites. *J. Eur. Ceram. Soc.* **2010**, *30*, 3111–3116. [CrossRef]
39. Wang, S.F.; Xia, M.G.; Liu, M.; Wang, Y.; Wang, B.; Bai, Y.; Wang, H.D. Finite element simulation of thermodynamic properties of NiCoCrAlY/YSZ gradient coating. *J. Aeronaut. Mater.* **2023**, *43*, 70–79.
40. Zhang, T.Y.; Wu, C.; Xiong, Z.; Zhou, S.F. Research progress in materials and preparation techniques of thermal barrier coatings. *Laser Optoelectron. Prog.* **2014**, *51*, 030004. [CrossRef]
41. Munro, R.G. Evaluated material properties for a sintered alpha-alumina. *J. Am. Ceram. Soc.* **1997**, *80*, 1919–1928. [CrossRef]
42. Bäker, M.; Fiedler, T.; Rösler, J. Stress evolution in thermal barrier coatings for rocket engine applications. *Mech. Adv. Mater. Mod. Process.* **2015**, *1*, 5. [CrossRef]

43. Bäker, M.; Seiler, P.A. Guide to Finite Element Simulations of Thermal Barrier Coatings. *J. Therm. Spray Technol.* **2017**, *26*, 1146–1160. [CrossRef]
44. Li, Z.; Chen, K.Y.; Jin, T. Finite element simulations of the thermomechanically coupled responses of thermal barrier coating systems using an unconditionally stable staggered approach. *Appl. Math. Model.* **2025**, *138*, 115750. [CrossRef]

Disclaimer/Publisher's Note: The statements, opinions and data contained in all publications are solely those of the individual author(s) and contributor(s) and not of MDPI and/or the editor(s). MDPI and/or the editor(s) disclaim responsibility for any injury to people or property resulting from any ideas, methods, instructions or products referred to in the content.